

Galaxy And Mass Assembly (GAMA): assimilation of KiDS into the GAMA database

Sabine Bellstedt¹★, Simon P. Driver^{1,2}, Aaron S. G. Robotham¹,
 Luke J. M. Davies¹, Kamran R. J. Bogue^{1,3}, Robin H. W. Cook¹,
 Abdolhosein Hashemizadeh¹, Soheil Koushan¹, Edward N. Taylor⁴,
 Jessica E. Thorne¹, Ryan J. Turner¹ and Angus H. Wright^{5,6}

¹ICRAR, The University of Western Australia, 35 Stirling Highway, Crawley, WA 6009, Australia

²SUPA, School of Physics & Astronomy, University of St Andrews, North Haugh, St Andrews KY16 9SS, UK

³School of Physics and Astronomy, Cardiff University, Queens Buildings, The Parade, Cardiff CF24 3AA, UK

⁴Centre for Astrophysics and Supercomputing, Swinburne University of Technology, Hawthorn, VIC 3122, Australia

⁵Astronomisches Institut, Ruhr-Universität Bochum, Universitätsstr. 150, D-44801 Bochum, Germany

⁶Argelander-Institut für Astronomie, Auf dem Hügel 71, D-53121 Bonn, Germany

Accepted 2020 May 21. Received 2020 May 8; in original form 2020 January 17

ABSTRACT

The Galaxy And Mass Assembly Survey (GAMA) covers five fields with highly complete spectroscopic coverage (>95 per cent) to intermediate depths ($r < 19.8$ or $i < 19.0$ mag), and collectively spans 250 deg^2 of equatorial or southern sky. Four of the GAMA fields (G09, G12, G15, and G23) reside in the European Southern Observatory (ESO) VST KiDS and ESO VISTA VIKING survey footprints, which combined with our *GALEX*, *WISE*, and *Herschel* data provide deep uniform imaging in the *FUV/NUV/u/g/r/i/Z/Y/J/H/K_s/W1/W2/W3/W4/P100/P160/S250/S350/S500* bands. Following the release of KiDS DR4, we describe the process by which we ingest the KiDS data into GAMA (replacing the SDSS data previously used for G09, G12, and G15), and redefine our core optical and near-infrared (NIR) catalogues to provide a complete and homogeneous data set. The source extraction and analysis is based on the new PROFOUND image analysis package, providing matched-segment photometry across all bands. The data are classified into stars, galaxies, artefacts, and ambiguous objects, and objects are linked to the GAMA spectroscopic target catalogue. Additionally, a new technique is employed utilizing PROFOUND to extract photometry in the unresolved MIR–FIR regime. The catalogues including the full FUV–FIR photometry are described and will be fully available as part of GAMA DR4. They are intended for both standalone science, selection for targeted follow-up with 4MOST, as well as an accompaniment to the upcoming and ongoing radio arrays now studying the GAMA 23^h field.

Key words: techniques: photometric – astronomical data bases: miscellaneous – catalogues – surveys.

1 INTRODUCTION

The era of the modern wide-area imaging survey, i.e. those based on linear digital detectors and covering a sizeable portion of the sky, started in earnest with the 2MASS¹ (Skrutskie et al. 2006), SDSS² (York et al. 2000), and UKIDSS³ (Lawrence et al. 2007) surveys – although it would be remiss not to mention the equally transformational IRAS⁴ (Neugebauer et al. 1984) and ROSAT⁵ (Voges et al. 1999) space missions. These programs, as well as achieving transformational science from the Solar System to the distant Universe, have, in turn, motivated the emergence of a multitude of dedicated imaging facilities on the ground including, for example,

SkyMapper (Keller et al. 2007); *VST*⁶ (Arnaboldi et al. 2007); *VISTA*⁷ (Sutherland et al. 2015); and *LSST*⁸ (Ivezić et al. 2019), and in space, for example, *GALEX*⁹ (Martin et al. 2005); *WISE*¹⁰ (Wright et al. 2010); *Spitzer* (Werner et al. 2004); *Herschel* (Pilbratt et al. 2010); *Euclid* (Beaulieu et al. 2010); and *Wide-Field Infrared Survey Telescope (WFIRST)*¹¹ (Gehrels et al. 2015) to highlight a few.

The further *federation* of these data streams with ground-based spectroscopy and other facilities has allowed for the construction of a truly multiwavelength and three-dimensional view of our Universe (e.g. Jarrett et al. 2017; Driver et al. 2018). In particular, major advances have been made in quantifying: the spatial distribution

* E-mail: sabine.bellstedt@uwa.edu.au

¹Two-Micron All-Sky Survey

²Sloan Digital Sky Survey

³UKIRT Infrared Deep Sky Survey

⁴Infrared Astronomical Satellite

⁵ROentgen SATellite

⁶VLT Survey Telescope

⁷Visible and Infrared Survey Telescope for Astronomy

⁸Large Synoptic Survey Telescope

⁹Galaxy Evolution Explorer

¹⁰Wide-field Infrared Survey Explorer

¹¹Wide-Field Infrared Survey Telescope

of galaxies and their use for cosmology; the distribution of groups and clusters; studies of galaxy populations; galaxy merger rates; the assembly of mass (stellar, dust, gas, and supermassive black holes); the transformation of mass; and identified the primary energy production pathways (star formation and active nuclei); all as a function of lookback time and environment. The data and science from these surveys now dominate our knowledge of the near and intermediate Universe, and provide the vital zero redshift benchmark for studies of the distant and adolescent Universe.

Not only has our knowledge and understanding been advanced, but also the way in which astronomy is conducted, shifting from an individual to team pursuit (Milojević 2014). Collectively, these *major* endeavours have allowed us to start the process of *comprehensively* mapping the evolution of all mass, energy, and structure over all cosmic time and to build the scaffolding upon which the numerical N -body, hydrodynamic, and semi-analytic models hang (e.g. Lagos et al. 2019). In the coming years such comprehensive studies will be massively augmented with new wide-area optical/near-infrared (NIR; *LSST*, *Euclid*, *WFIRST*), X-ray (*eROSITA*), and deep radio (MeerKAT, ASKAP, MWA, and SKA) imaging and spectral surveys, taking us from a multiwavelength outlook, to a truly panchromatic perspective.

While acknowledging this impending paradigm shift from a mono- to pan-facility culture, it is worth noting that the majority of all photons produced, since mass–energy decoupling (by energy or number), arise in the ultraviolet, optical and NIR regimes (see the recent summary of the extragalactic background by Hill, Masui & Scott 2018). Half of these photons are predominantly produced by stars and through star formation, and the other half are produced through the accretion of baryonic material on to supermassive black holes. One important caveat is that almost half of these freshly minted photons (Dunne et al. 2003; Driver et al. 2016c, b) are almost immediately attenuated by dust grains, which reradiate the energy into the far-infrared (FIR), before it emerges from the host galaxy. Including the shifting of wavelengths longward due to the expansion, the implication is that when building our panchromatic perspective, one might wish to start where photon production is dominant and readily detectable (i.e. the optical/NIR) and where, arguably, the information content is highest.

Here, we describe the construction of a new deep optical/NIR imaging data set, built upon two ESO Public Surveys (VST KiDS¹² and VISTA VIKING; Arnaboldi et al. 2007; de Jong et al. 2013b) combined with the Galaxy And Mass Assembly (GAMA) panchromatic and spectroscopic survey (Driver et al. 2011; Hopkins et al. 2013; Liske et al. 2015; Driver et al. 2016b). In particular, a key 50 deg² region (G23/WD23; see Driver et al. 2019), will be targeted for future high-density spectroscopic, X-ray spectral, and radio line and radio continuum observations. The data set presented herein, and including all unique GAMA redshifts, therefore forms the basis upon which to grow our panchromatic perspective.

At its core, the GAMA survey (Driver et al. 2011; Liske et al. 2015), spanning five fields, is a spectroscopic Legacy campaign using the Anglo Australian Telescope’s AAOmega wide-field facility (see Hopkins et al. 2013). The five fields are each ~ 50 – 60 deg² in extent, and located at: 2^h (G02), 9^h (G09), 12^h (G12), 14.5^h (G15), and 23^h (G23). The G09, G12, and G15 fields lie in the equatorial North Galactic Cap region, and have similar properties in terms of depth of the spectroscopic follow-up ($r < 19.8$ mag), area (60 deg²), spectroscopic completeness (98 per cent), and panchromatic coverage (UV

to FIR; Driver et al. 2016b). The bulk of the GAMA science to date is based on the analysis of these three fields. The original GAMA G02 field overlaps with the VIPERs and XMM–XXL equatorial field, and covers 55.7 deg² in extent. The field was not completed, however, a 19.5 deg² sub-region attained uniform 95.5 per cent spectroscopic completeness to $r < 19.8$ mag (see Baldry et al. 2018).

The final GAMA field at 23^h and $-32^\circ 5'$, lies in the Southern Galactic Cap, with a spectroscopic survey limit of, $i < 19.0$ mag, but with a slightly lower completeness of 94 per cent (see Liske et al. 2015). To date, little science has been based on the G23 region (although see studies such as Bilicki et al. 2018; Vakili et al. 2019, for examples, where these data have been used), however, in due course it represents our premier field, because of its suitability for southern hemisphere follow up. In particular, this follow-up will be conducted by radio facilities, and a deep spectroscopic extension is planned as part of the Wide Area VISTA Extra-galactic Survey (WAVES); one of ten core surveys to be conducted by the 4MOST Consortium (see de Jong et al. 2019; Driver et al. 2019). This will extend the G23 region at high spectroscopic completeness (> 90 per cent), to a limit of $m_z \leq 21.2$. In addition, WAVES will also survey the full KiDS region ($m_z \leq 21.2$, $z_{\text{phot}} < 0.2$), and the LSST Deep-Drill fields ($m_z \leq 21.2$, $z_{\text{phot}} < 0.8$). Note that object selection for the WAVES-wide survey will be conducted using joint KiDS and VIKING photometry.

In preparation, the G23/WD23 region is being extensively observed by Southern Hemisphere located radio facilities including: the Australian Compact Array (ATCA) as part of the GAMA Legacy ATCA Sky Survey (Hyunh et al. in preparation), the Australian Square Kilometre Array Pathfinder (Leahy et al. 2019) as part of the EMU¹³ (Norris et al. 2011), DINGO¹⁴ (Meyer et al. in preparation) and FLASH¹⁵ (Allison et al. 2020) surveys, and by the Murchison Wide-Field Array GOLD and MIDAS surveys (Seymour et al. in preparation). The expectation is that the G23/WD23 region, with its exceptionally high-density and deep spectroscopic completeness, should be a suitable location for a medium-deep survey, with upcoming facilities such as the Vera Rubin Observatory,¹⁶ the Square Kilometer Array (SKA), *Euclid*, and *WFIRST*.

In terms of panchromatic imaging, G23/WD23 currently has comparable coverage to the GAMA equatorial fields, with data arising from concerted *GALEX* (NUV), VST KiDS, VISTA VIKING, *WISE*, and *Herschel* imaging campaigns. This wealth of data, combined with radio observations, and future upcoming deep spectroscopic observations, makes G23 a field of interest in coming years for extensive follow-up of either the entire field, or well-selected sub-samples.

In Section 2, we describe the assimilation of the KiDS data into the GAMA Panchromatic Database followed by the generation of the base source catalogues from far-ultraviolet (FUV) to W2 using the new ProFound image analysis package (Robotham et al. 2018). In Section 3, we use PROFOUND PSF-convolution mode to obtain photometry from W3 through to the PACS and SPIRE far-IR bands for objects brighter than $r \sim 20.5$ mag. In Section 4, we verify the zero-points, astrometry, and compare our revised photometry to our previous LAMBDA-based photometry. This includes verification of the zero-points and astrometry, star masking using GAIA DR2, Galactic extinction corrections using *Planck*, star–galaxy separation based on colour and size, extensive visual

¹²Kilo Degree Survey

¹³Evolutionary Map of the Universe

¹⁴Deep Investigation of Neutral Gas Origins

¹⁵First Large Absorption Survey in H I

¹⁶Formerly referred to as the Large Survey Synoptic Telescope (LSST)

inspection, and comparisons to earlier data. In Section 5, we provide information on how to access the catalogues, and, in particular, provide some example extractions. Two companion papers describe the search for low-surface brightness galaxies within the data set (Turner et al. in preparation), and the use of the panchromatic data to reconstruct the star formation history of individual galaxies and sub-populations via a ‘forensic’-style analysis (Bellstedt et al. 2020). Further, papers incorporating radio observations are in preparation.

All magnitudes reported here are in the AB system and when necessary we assume a cosmology with $H_0 = 70 \text{ km s}^{-1} \text{ Mpc}^{-1}$, $\Omega_m = 0.3$, and $\Omega_\Lambda = 0.7$.

2 ASSIMILATION OF VST KIDS INTO THE GAMA PANCHROMATIC DATA BASE

The target catalogues to the GAMA spectroscopic campaign were built upon three distinct optical surveys: the Sloan Digital Sky Survey (SDSS; G09, G12, and G15), the Canada–France Legacy Survey (CFHTLS; G02), and the European Southern Observatory’s VLT Survey Telescope’s Kilo-degree Survey (KiDS; G23). For the equatorial regions, the GAMA input catalogue is described in detail in Baldry et al. (2010) and for the G02 region is described in Baldry et al. (2018). The G23 input catalogue, used for the GAMA spectroscopic survey, has not been described previously and in brief, was constructed in 2014 based on initial pre-release VST KiDS data. These data have since undergone a number of revisions in terms of re-determination of the photometric zero-points, replacement of low-quality data frames, and the filling in of data gaps as the KiDS team have honed their reduction and analysis pipelines. Nevertheless, our early KiDS analysis resulted in an *i*-band limited target catalogue ($i < 19.0$ mag), with star–galaxy separation based on table-matched NIR colours and size estimates, augmented with extensive and fairly ad hoc visual checks (based on selections designed to identify artefacts and ensure no galaxies were misclassified as stars). This initial input catalogue is available from the GAMA database and, while not ideal nor optimal, formed the basis for spectroscopic observations with the AAOmega facility on the AAT from 2014–2016 (see Liske et al. 2015).

Since this time the VST KiDS team has completed *ugri* coverage of the three GAMA equatorial fields, and the G23/WD23 field. These data have recently been released as part of VST KiDS DR4,¹⁷ (Kuijken et al. 2019) and provide near complete coverage in all bands across the four primary GAMA fields. In one region of G23, the DR4 data are missing, however, data exist from the earlier DR3 release and so we include these three fields. We are hence now in a position to redefine the GAMA base optical/NIR catalogues in a uniform manner across our four primary regions. In doing so, we create both deeper, and higher resolution imaging, from which we can derive more robust flux, size measurements, and derived parameters (e.g. stellar masses, star formation rates, and photometric redshifts). The main purpose of this paper is to provide a record of this replacement process – a process akin to swapping the tablecloth on a fully laid table.

KiDS DR4 data are downloadable from the ESO archive, and come pre-SWARPed (Bertin 2010) into 1 deg^2 tiles. These are astrometrically and photometrically calibrated by the KiDS team using, initially, the Sloan Digital Sky Survey in the North and 2MASS in the South, and with further supplementary calibration to GAIA DR2 *g*, as part of the final DR4 calibration process. Note that the

DR4 data tiles as released, contain both a zero-point for each tile (PHOTZ), reflecting the initial calibration, and, a further zero-point offset (DMAG) to adjust any derived flux measurements to the GAIA DR2 *g*-band system. Our initial action is therefore to modify all DR4 tiles to absorb the DMAG correction into the specified zero-points, by scaling the data. This is done to legitimately mosaic tiles, allowing for the construction of KiDS maps at any location and any size within the KiDS footprint.

We now follow the procedure outlined in the GAMA Panchromatic Data Release (PDR; Driver et al. 2016b) and build large single SWARP (Bertin 2010) images for each GAMA region. These (very) large mosaics are available via the Panchromatic SWARP Imager¹⁸ (Driver et al. 2016b). We discuss the revised panchromatic depth of this imaging in Section 4. In total, we SWARP 280 deg^2 tiles from KiDS, and also take the opportunity to rebuild our VIKING SWARPs using additional data amounting to 129 869 VISTA detectors (see Koushan et al. in preparation, for details on the VISTA VIKING data). This comprises a total data volume of 3.44TB and all mosaics are available via the URL indicated above and via the Public Data Central portal.¹⁹ Images showing a visual comparison of KiDS and SDSS data are provided in fig. 1 of Turner et al. (in preparation).

2.1 The adoption of ProFound for source detection – a brief digression

In constructing the PDR (Driver et al. 2016c), we made use of the original source detection as provided by the SDSS Data Release 6, within our survey footprint. Following star–galaxy separation based on colour and size criteria (Baldry et al. 2010), these data were used to define the GAMA input catalogue for the GAMA spectroscopic survey of the three equatorial fields, undertaken on the Anglo-Australian Telescope from 2011 to 2016 (see Liske et al. 2015). The original SDSS-derived equatorial input catalogue was later table matched to our independent *r*-band catalogues, determined using SOURCE EXTRACTOR (Bertin & Arnouts 1996). SOURCE EXTRACTOR was then applied in dual-band mode to determine forced aperture photometry from *u* to *K_s*, using the elliptical apertures defined by SOURCE EXTRACTOR. Further table matching to independent catalogues in *GALEX*, *WISE*, and *Herschel* bands resulted in the far-UV to far-IR publicly available PDR data set.²⁰ This catalogue was later superseded by flux measurements also based on our *r*-band defined apertures but now using the LAMBDA in-house software (Wright et al. 2016) to measure forced photometric fluxes in all 21 bands (covering ultraviolet (UV) to IR wavelengths) following convolution of the initial aperture with the relevant facility point spread function.

Throughout this process, a number of important lessons related to galaxy photometry emerged. First, the undesirable reliance on table-matching to connect the SDSS input catalogue to our LAMBDA photometry, which inherently introduces errors due to different deblending outcomes between the SDSS IMAGING PIPELINE and SOURCE EXTRACTOR methodologies. Secondly, issues arose around the integrity of the SOURCE EXTRACTOR aperture definitions. In particular, SOURCE EXTRACTOR, like most detection algorithms, can be prone to bright galaxy fragmentation, and in some cases highly erroneous apertures, often due to the defined aperture following an isophotal bridge and looping round a nearby bright star – these

¹⁸<https://datacentral.org.au/services/cutout/>

¹⁹<http://datacentral.org.au/>

²⁰<https://datacentral.org.au/services/cutout/>

¹⁷<http://kids.strw.leidenuniv.nl/>

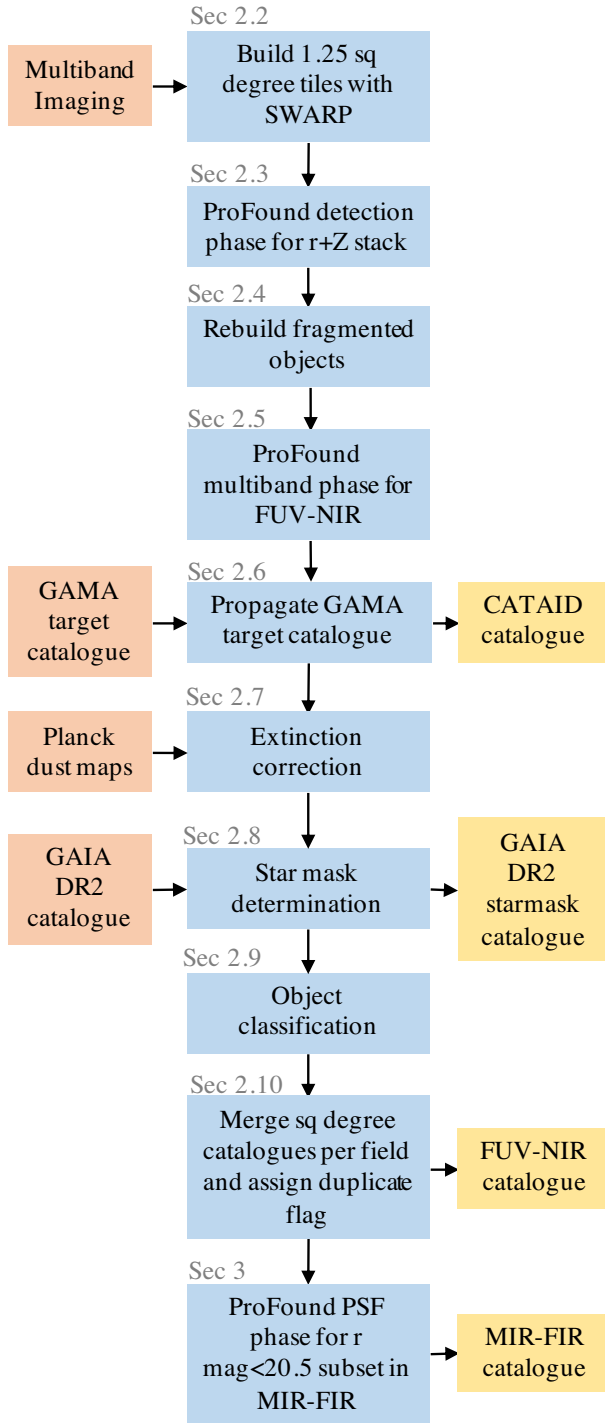


Figure 1. Workflow for the adopted pipeline. Inputs to the pipeline are shown in orange, steps of the pipeline in blue, and outputs in yellow.

issues arise because of the difficulty in simultaneously measuring fluxes for both very bright and very faint sources. Similar issues were also identified in our re-analysis of panchromatic photometry in the G10/COSMOS field (Andrews et al. 2017). Following the visual assessment of all GAMA apertures, via a citizen science project, it became apparent that typically 10 percent of all apertures did not define the object to the desired level of accuracy.

This led to the development of a new source finding code,²¹ PROFOUND (Robotham et al. 2018), with three important philosophical changes in source finding. First, instead of using circular (SDSS IMAGING PIPELINE), or elliptical (SOURCE EXTRACTOR) apertures, PROFOUND acknowledges that most galaxies have irregular shapes, particularly as one probes to higher redshifts, fainter isophotal levels, and closer to the confusion limit. The PROFOUND software identifies and preserves the initial isophote (or segment), which may be regular or irregular in shape. Secondly, we introduced the concept of segment dilation (akin to a curve of growth) to obtain pseudo-total fluxes through the sequential addition of layers of pixels surrounding each segment. This process continues until the flux converges (in our case defined by a less than 5 percent increase in flux), or the maximum number of allowable dilations is reached, resulting in pseudo-total magnitude estimates. Thirdly, SOURCE EXTRACTOR uses a hierarchical or nested-deblend process, by which derived elliptical apertures may overlap, and hence where flux can be double counted if not managed appropriately in later analysis. In the PROFOUND software package, a watershed deblending approach is taken, where during the dilation process segments are not allowed to overlap – i.e. all the flux in any one pixel is allocated to one object only.

One can argue in specific cases as to which deblend approach, nested or watershed, is more appropriate, e.g. a nested approach is better for a small satellite within a large halo, while a watershed approach is better for dense complexes, or as one approaches the confusion limit. Our experience is that the watershed approach behaves better when things go pathologically wrong – i.e. it is the least worst of the two approaches for difficult cases. For full details on PROFOUND see the code description paper Robotham et al. (2018), or recent applications to the deep DEVILS imaging data from VISTA VIDEO (Davies et al. 2018). In the sections that follow we will adopt and apply ProFound and develop a pipeline around it to manage the multitude of issues that arise with wide-area data collected from multiple ground-based facilities. We show the adopted workflow for the pipeline presented within this paper in Fig. 1.

2.2 Building 1.25 deg² overlapping tiles with SWARP

Prior to running PROFOUND on KiDS and VIKING data, we first use the SWARP package (Bertin 2010) to build slightly extended 1.12×1.12 deg² images in each band (*FUV*, *NUV*, *u*, *g*, *r*, *i*, *Z*, *Y*, *J*, *H*, *K_s*, *W1*, *W2*, *W3*, *W4*, *P100*, *P160*, *S250*, *S350*, *S500*) – essentially adding overlap regions. A summary of the imaging data used in each band is provided in Table 1, including the data source, coverage area, depth, median seeing and zero-point values. These revised tiles are centred on the rescaled KiDS 1 deg² tiles sourced from the ESO archive. In SWARPing the data, we regrid all bands to a resolution of 0.339 arcsec, use a background smoothing mesh of 256×256 (pixels), and a background filter size of 3×3 (background cells). The data frames are combined using the MEDIAN combine option, which we have deemed to be the most stable option for regions with poor-quality data.

Fig. 2 shows an example of a SWARPed tile indicating the depth and quality in each band. Visual inspection was made of all data frames, using images similar to Fig. 2, to ensure each tile in each band was correctly built. In some cases, it was noted that the individual tiles provided by KiDS were missing detectors in some bands, and in some tiles, which will leave gaps in the panchromatic coverage. Objects with missing coverage in a particular band

²¹ Available on Github: <https://github.com/asgr/ProFound>

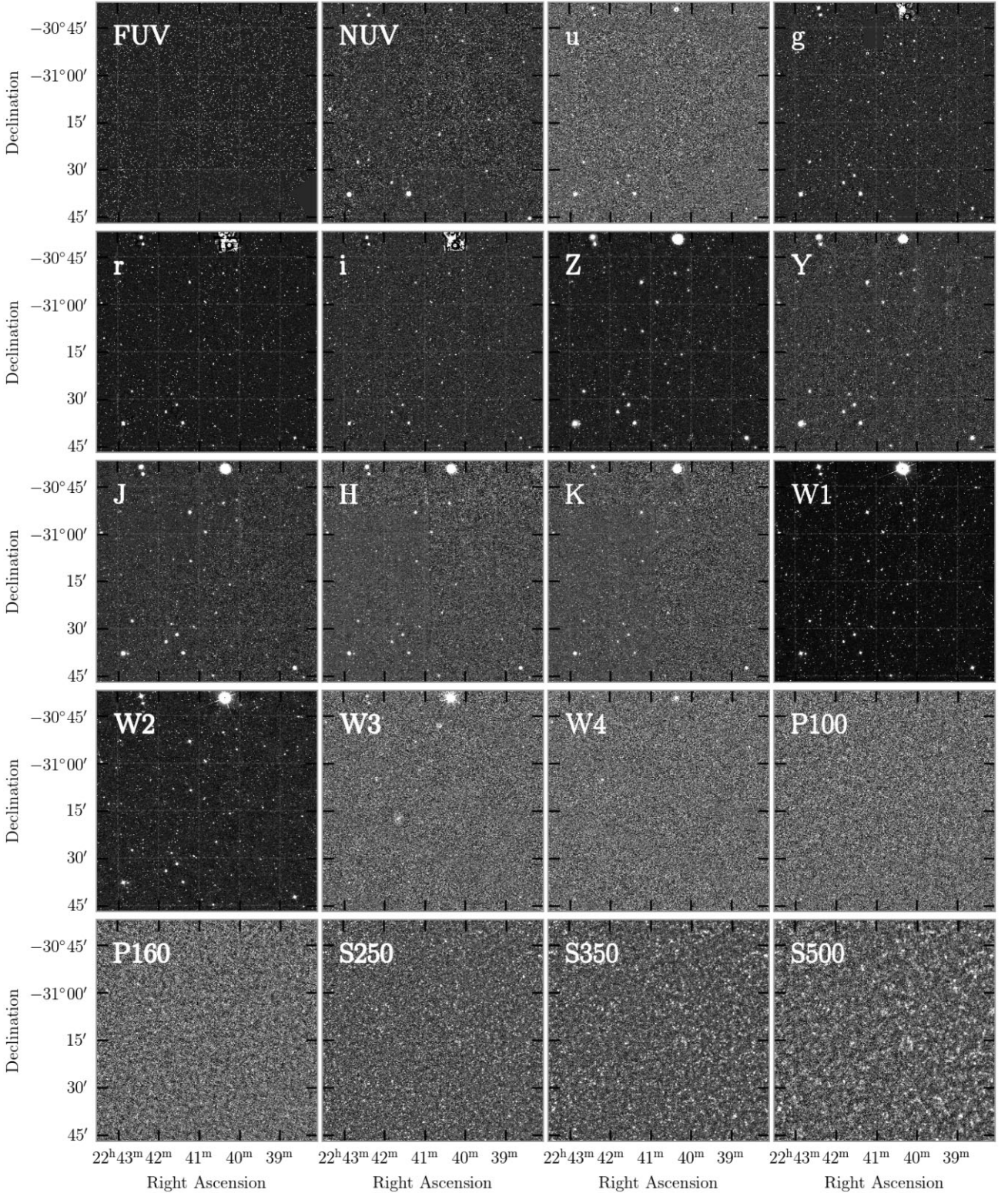


Figure 2. Each frame shows a SWARPed $1.12 \times 1.12 \text{ deg}^2$ TILE for the band indicated in the top left-hand panel. Similar images were used to inspect the full data set and record any pertinent issues, such as the missing detector in the *g* TILE above.

will have fluxes and magnitudes set to either NA or -999. Based on a visual inspection of the image quality, we conclude that a PROFOUND analysis based on combined *r* + *Z* stacks will provide

near complete and contiguous coverage over all four GAMA regions.

Table 1. Summary of key statistics for the imaging data sets used in each of the photometric bands used in this release. Limits provided by Driver et al. (2016c) indicate the range of values over the four GAMA fields.

Band	Central wavelength	Instrument	Data set/survey	Area (deg ²)	Limits (AB mag)	Median seeing (arcseconds)	Zero-point (AB mag for 1 ADU)
<i>FUV</i>	1 539 Å	<i>GALEX</i>	MIS + GO ^a	186.74	24.59–26.40 ^g	N/A	18.82
<i>NUV</i>	2 316 Å	<i>GALEX</i>	MIS + GO ^a	204.3	23.64–24.07 ^g	N/A	20.08
<i>u</i>	3 582 Å	VST	KiDS ^b	211.21	24.8 ^a	0.9–1.1 ^b	0
<i>g</i>	4 760 Å	VST	KiDS ^b	211.21	25.4 ^a	0.7–0.9 ^b	0
<i>r</i>	6 326 Å	VST	KiDS ^b	211.21	25.2 ^a	<0.6 ^b	0
<i>i</i>	7 599 Å	VST	KiDS ^b	211.21	24.2 ^a	<1.1 ^b	0
<i>Z</i>	8 854 Å	VISTA	VIKING ^c	211.21	23.04–23.19 ^g	1.0 ^d	30
<i>Y</i>	10 229 Å	VISTA	VIKING ^c	211.21	22.34–22.51 ^g	1.0 ^d	30
<i>J</i>	12 556 Å	VISTA	VIKING ^c	211.21	22.06–22.21 ^g	0.9 ^d	30
<i>H</i>	16 499 Å	VISTA	VIKING ^c	211.21	21.33–21.42 ^g	1.0 ^d	30
<i>K_S</i>	21 571 Å	VISTA	VIKING ^c	211.21	21.30–21.48 ^g	0.9 ^d	30
<i>W1</i>	3.40 µm	WISE	AllSky ^e	211.21	21.09–21.41 ^g	N/A	23.16
<i>W2</i>	4.65 µm	WISE	AllSky ^e	211.21	20.26–20.77 ^g	N/A	22.82
<i>W3</i>	12.8 µm	WISE	AllSky ^e	211.21	18.44–18.89 ^g	N/A	23.24
<i>W4</i>	22.4 µm	WISE	AllSky ^e	211.21	16.54–16.96 ^g	N/A	19.6
<i>P100</i>	98.9 µm	PACS	ATLAS ^f	211.21	12.96–13.14 ^g	N/A	8.9
<i>P160</i>	156 µm	PACS	ATLAS ^f	211.21	13.44–13.66 ^g	N/A	8.9
<i>S250</i>	249 µm	SPIRE	ATLAS ^f	181.14	12.52–12.60 ^g	N/A	11.68
<i>S350</i>	350 µm	SPIRE	ATLAS ^f	181.14	12.36–12.51 ^g	N/A	11.67
<i>S500</i>	504 µm	SPIRE	ATLAS ^f	181.14	12.16–12.23 ^g	N/A	11.62

^a Martin et al. (2005), ^b de Jong et al. (2013b), de Jong et al. (2013a), ^c Edge et al. (2013), Venemans et al. (2015), ^e Wright et al. (2010), ^f Eales et al. (2010), ^g Driver et al. (2016c).

2.3 Source detection with PROFOUND

Source detection is conducted via the PROFOUND package (Robotham et al. 2018). This is based on PROFOUND version 1.10.8, which can be obtained from <https://github.com/asgr/ProFound>. Within PROFOUND numerous parameters exist that determine the manner in which sources are extracted from the image. For completeness, we show the exact command we use in the Appendix using the PROFOUNDMULTIBAND command. The command allows the user to specify one or more bands to use for the detection pass as well as the bands for which measurements should be made. In the initial source detection phase, only the detection bands are provided. When multiple images are specified for detection they are combined in an inverse variance weighting based on the internal background assessment. Here, we combine data from the KiDS *r* band and the VIKING *Z* band, i.e. *r* + *Z*. This has the distinct advantage of overcoming some artefact effects such as ghosting, satellite trails, and bad pixels. Fig. 3 shows a KiDS VST *r*-band image (upper), a VISTA VIKING image (middle), and the combined *r* + *Z* image (lower).

Inherent to PROFOUND, is its robust modelling of the local background, which may include the sky, the haloes of bright objects, scattered light or artificially enhanced regions, through appropriate median filtering (see Robotham et al. 2018). Fig. 4 shows an example TILE with the original image (left-hand panel), the derived background map (centre panel, where the background is seen to be elevated near the positions of bright objects, particularly bright ghosting), and the sky root-mean sky statistics (right, again indicating regions of heightened uncertainty in the background estimate). This information is used in determining flux errors, ensuring objects in noisier regions have appropriately derived errors. In examining the background in detail the genesis of the data is also apparent in the Sky Root Mean Square (SkyRMS) map (right-hand panel). This is a common feature in surveys we have

studied, and in this case highlights the varying noise characteristics of the individual detectors going into the initial SWARP TILE image.

2.4 Rebuilding fragmented galaxies

A common problem in most automated detection algorithms is that of fragmenting of bright galaxies. To check this, we select all known galaxies from the Third Reference Catalogue (RC3; de Vaucouleurs et al. 1991) that lie within the GAMA regions, and produce cutout images with the derived segments overlain. There are 21, 144, 31, and 10 RC3 galaxies within the G09, G12, G15, and G23 regions, respectively. Note that the G12 region includes the Virgo Southern Spur, and G23 includes a nearby void region. Initial investigations showed that PROFOUND also tended to overly fragment very bright galaxies. Two enhancements were implemented in PROFOUND to assist with this.

One new parameter on top of the standard TOLERANCE threshold (which determines how much peak flux an object needs relative to neighbouring objects before being merged) is RELTOL. This modifies the TOLERANCE by the ratio between the segment peak flux and the saddle point flux where it touches a neighbouring segment to the power of RELTOL. Since the default is RELTOL=0, this will, in general, have no effect. However, when it is made larger than 0 merging becomes more aggressive in the outskirts of galaxies where the peak flux will tend to be much larger than the saddle point flux. Subjectively, raising this above 0 tends to do a better job of keeping very extended and flocculent spiral galaxies intact, and it has a little negative impact on the fainter source deblending that parameters will tend to be optimized for (since this is where most of our survey sources exist).

The other new parameter to better control segmentation is CLIPTOL. This specifies the saddle point flux above which segments are always merged, regardless of competing criteria. For very bright objects

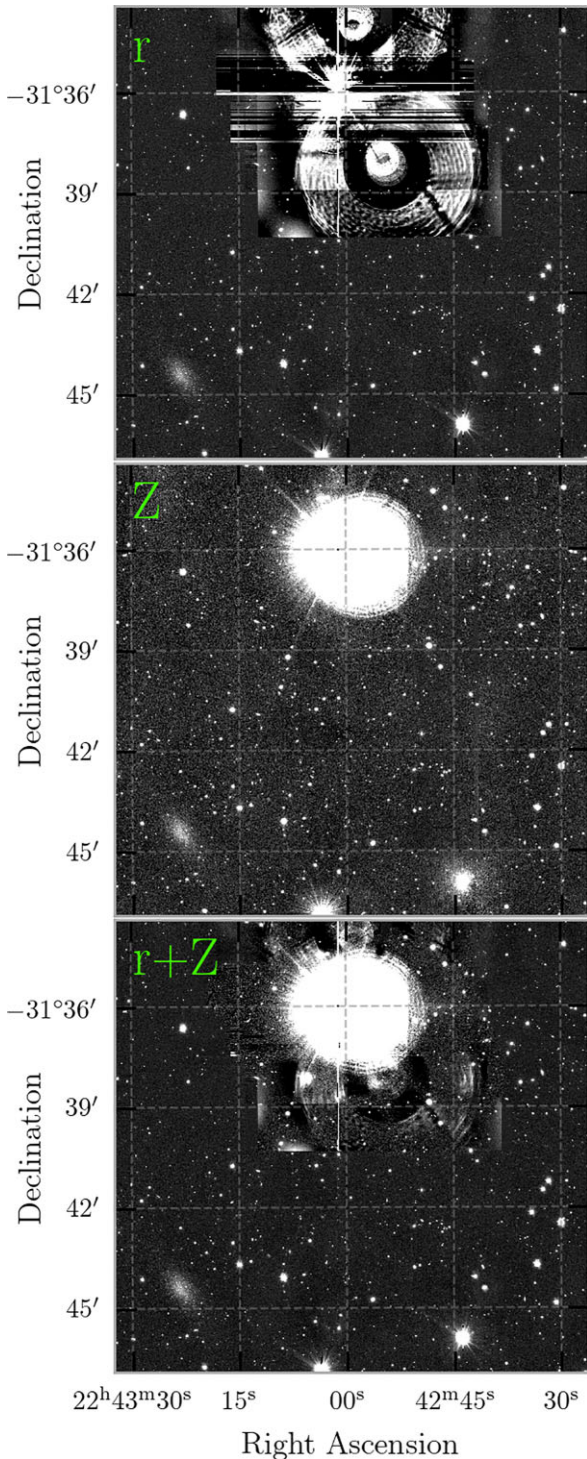


Figure 3. The above panel shows a section from the top mid-region of Fig. 2 VST KiDS r frame (top panel) and a VISTA VIKING Z frame (middle panel) and the combined stack weighted by inverse noise variance (bottom panel). A problem region is shown indicating how the use of two frames from different telescopes helps to mitigate issues due to stellar ghosting.

with complex image artefacts (e.g. around bright stars), this proves to be very successful at properly reconstructing sources, which might otherwise be significantly fragmented due to the presence of spurious flux discontinuities. Given most applications will apply a bright starmask, this option is perhaps somewhat cosmetic, but it does mean

PROFOUND will return reasonable photometry even for the brightest and most difficult sources.

As this fragmentation was occurring despite the new PROFOUND parameters, a process was implemented to manually regroup segments that belong to a single object. To complete this task, an in-house tool was developed that allowed users to view a thumbnail of an object and click on segments to be regrouped. This tool is available through the `profoundSegimFix` function within PROFOUND. An example of an object whose segments have been merged in this way can be seen in Fig. 5, where the right panel shows the resulting segmentation map after merging. Per square degree, an output file was produced that recorded which segments (as determined by the detection phase of PROFOUND) needed to be regrouped.

Rather than visually inspecting every object, only objects with three or more abutting segments, a total group²² magnitude <20.5 , and groups not flagged as containing a star were selected to be visually checked. For the full GAMA sample, this resulted in 75 863 objects. Of these, 6 777 required manual intervention. In total, this task took a week, with seven authors (SB, SPD, AR, LJD, JT, RC, CB, HH) assisting in the regrouping process.

Before running the multiband form of PROFOUND, the manual fixes to segments were applied to the detected segmentation map using the command `profoundSegimKeep`. This fixed segmentation map was used for the remainder of the photometry pipeline.

2.5 Multiband Photometry with PROFOUND

After initial segments (isophotal outlines) are defined from the stacked r and Z image (as described in Section 2.3) and have been fixed for fragmentation (as described in Section 2.4), the fixed segments then form the basis for subsequent measurements in the analysis bands (FUV , NUV , u , g , r , i , Z , Y , J , H , K_s , $W1$, $W2$).

Within each band, flux measurements are presented in two different ways. In order to account for all of the flux of a single object, individual segments require dilation beyond the detected segment. Dilation is conducted iteratively, where the edges are extended until all object flux has been accounted for. The background sky estimate is made as both a global sky measurement, or a local sky measurement, where the sky is measured within the dilated annulus. The resulting flux when using the global sky measurement for sky subtraction is indicated as $FLUX_T$ in the catalogue, whereas the flux resulting from a local sky subtraction is indicated as $FLUX_L$. For large objects with significant halo flux, a local sky subtraction is liable to subtracting off the halo light, and therefore the $FLUX_T$ measurement is expected to better represent the total galaxy flux. Conversely, for very faint galaxies (particularly those that are close to noisy regions), we expect that the $FLUX_L$ measurement will best represent the galaxy flux. For the sake of selection cuts in the remainder of the paper, we have utilised the $FLUX_T$ measurement.

The flux errors derived by PROFOUND include the errors due to sky subtraction and sky rms (as outlined in Section 2.3). Whilst it is also possible for PROFOUND to derive the error contribution by pixel noise correlation (introduced through the SWARP pixel resampling process), we have not included this contribution in our analysis as it contributes only a small (often negligible) fraction of the error introduced by the sky and sky rms. Based on tests for a single square degree, we find that the median pixel correlation contribution to the flux error is highest

²²In the context of the photometry, *group* refers to a collection of segments directly abutting each other.

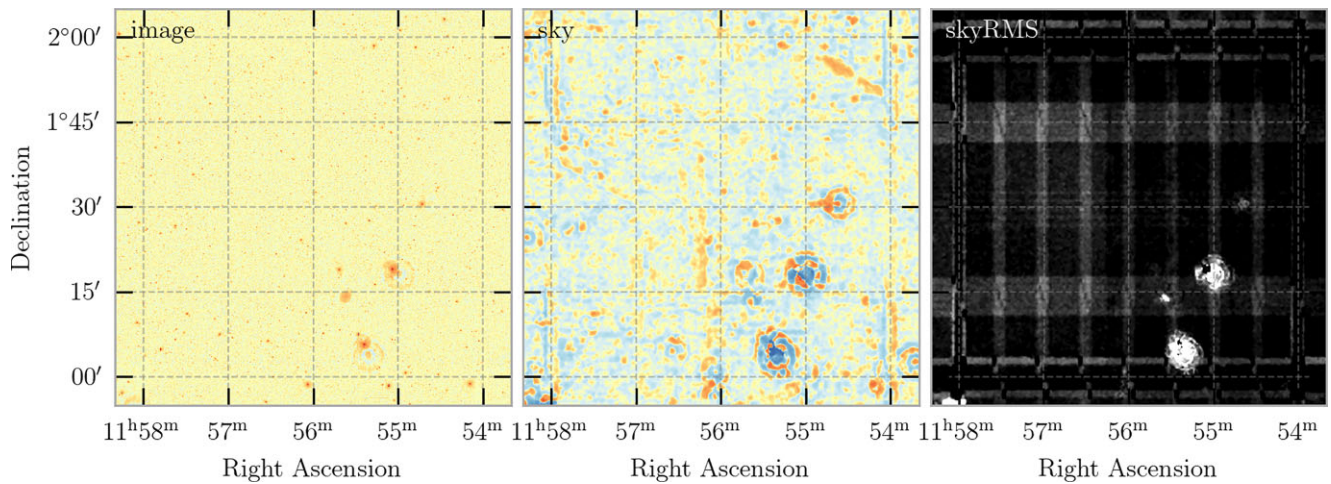


Figure 4. ProFound’s inbuilt background analysis, showing the original deg^2 data (left-hand panel), the derived background sky map (centre panel), and the derived background root mean square map (right-hand panel).

in the *NUV*/*W1*/*W2* bands with 11/12/8 per cent, respectively, but overall it is much smaller, with a mean contribution of 3 per cent over all bands. The error due to pixel correlation is expensive to compute, therefore omitting this uncertainty contribution saves significant computational time. We refer the reader to Robotham et al. (2018) for the details on uncertainty derivation in PROFOUND.

For completeness, we show the `profoundMultiBand` command used to derive our multiband catalogues for each SWARPed tile in the Appendix. This amounts to the production of 280 distinct catalogues each containing around 300 000 objects and taking about 12 h to build the SWARPs, and a further 6 h to process PROFOUND. The software is hence run on the Pawsey Supercomputing Centre’s Zeus machine, taking about 2 d to complete a full run across all tiles.

2.6 Linking to GAMA objects

To link the new photometric catalogue to the existing GAMA target catalogue (which contains 1 468 620 objects across all four GAMA fields), we project the GAMA catalogue on to the PROFOUND segments. A successful projection will occur if a GAMA coordinate is encompassed by a corresponding PROFOUND segment. In some cases (44 766 instances over all four fields), a single PROFOUND segment is linked to more than one GAMA input object. This generally occurs if multiple GAMA targets were placed on a single object, but can also occur if two objects have not been appropriately deblended by PROFOUND, and hence share a segment. Two strategies are implemented in order to decide which GAMA ID should be assigned to the segment when a single segment coincides with multiple GAMA objects. If the GAMA objects have spectroscopically measured redshifts, then the selected ID is taken to be the object whose redshift is closest to the flux-weighted mean redshift of all GAMA objects present in the segment. If redshift measurements do not exist, however, then the selected ID is taken from the object contributing the largest amount of flux to the segment.

For individual cases where a segment contains multiple GAMA sources that have redshifts varying by more than 0.1, we allocate a flag `Z_CONFUSIONFLAG=1`. This assists in the identification of objects for which the redshift measurement is not indicative of all the flux in the segment.

2.6.1 Objects in KiDS/VIKING not in GAMA

After matching our final KiDS/VIKING catalogue to the GAMA input catalogue (which extends to $r_{\text{GAMA}} = 21.0$ mag), we cut the catalogue at $r_{\text{KiDS}} < 20$ mag (just beyond the GAMA spectroscopic limit of $m_r = 19.8$). This identifies almost 11 000 galaxies not previously recorded. Visual inspection of all ~ 11 000 reveals that ~ 6 000 of these objects are artefacts not previously flagged, ~ 3 000 are galaxies not previously identified, and the remaining objects are equally divided between stars or ambiguous objects. In total, these objects represent < 1 per cent of the galaxies above this flux limit but nevertheless we introduce an eyeball flag `EYECLASS` so that these objects can be indicated. We also introduce an `UBERCLASS` flag which takes as its value the `EYECLASS` if known or the `CLASS` flag if not known. We therefore recommend the `UBERCLASS` flag be used to extract star, galaxy and/or ambiguous subsets. In addition to the previously missed galaxies, we identify a mixture of low surface brightness systems, and objects that have been identified as the close pair of a previously identified galaxy, but had not been separately resolved in the past. In a companion paper, Turner et al. (in preparation), we provide more detail on these objects and discuss the implications for the stellar mass density.

2.6.2 Objects in GAMA not in KiDS/VIKING

Similarly, we can also identify objects in the GAMA spectroscopic target catalogue ($r_{\text{GAMA}} < 19.8$ mag) that are not matched in the new KiDS/VIKING catalogues. Either, a non-match arises from the fact that no object has been identified at the coordinate of the GAMA object, or because multiple GAMA objects have been engulfed by a single segment, resulting in only a portion of the GAMA objects appearing in the final catalogues. Within the four GAMA fields, 16 068 objects have been identified for which no object has been detected in the KiDS/VIKING photometry, and in almost all cases this is because the GAMA object points to a sky position in our updated photometry. This is likely an indication that the original SDSS photometry on which the GAMA input catalogue was based contained some sort of artefact at these coordinates. Only ~ 150 of these GAMA targets have securely measured redshifts, and these objects fall within regions that are missing imaging in $r + z$, and hence do not appear in the new KiDS/VIKING catalogues. Finally, 44 766 objects have been identified within the new catalogues

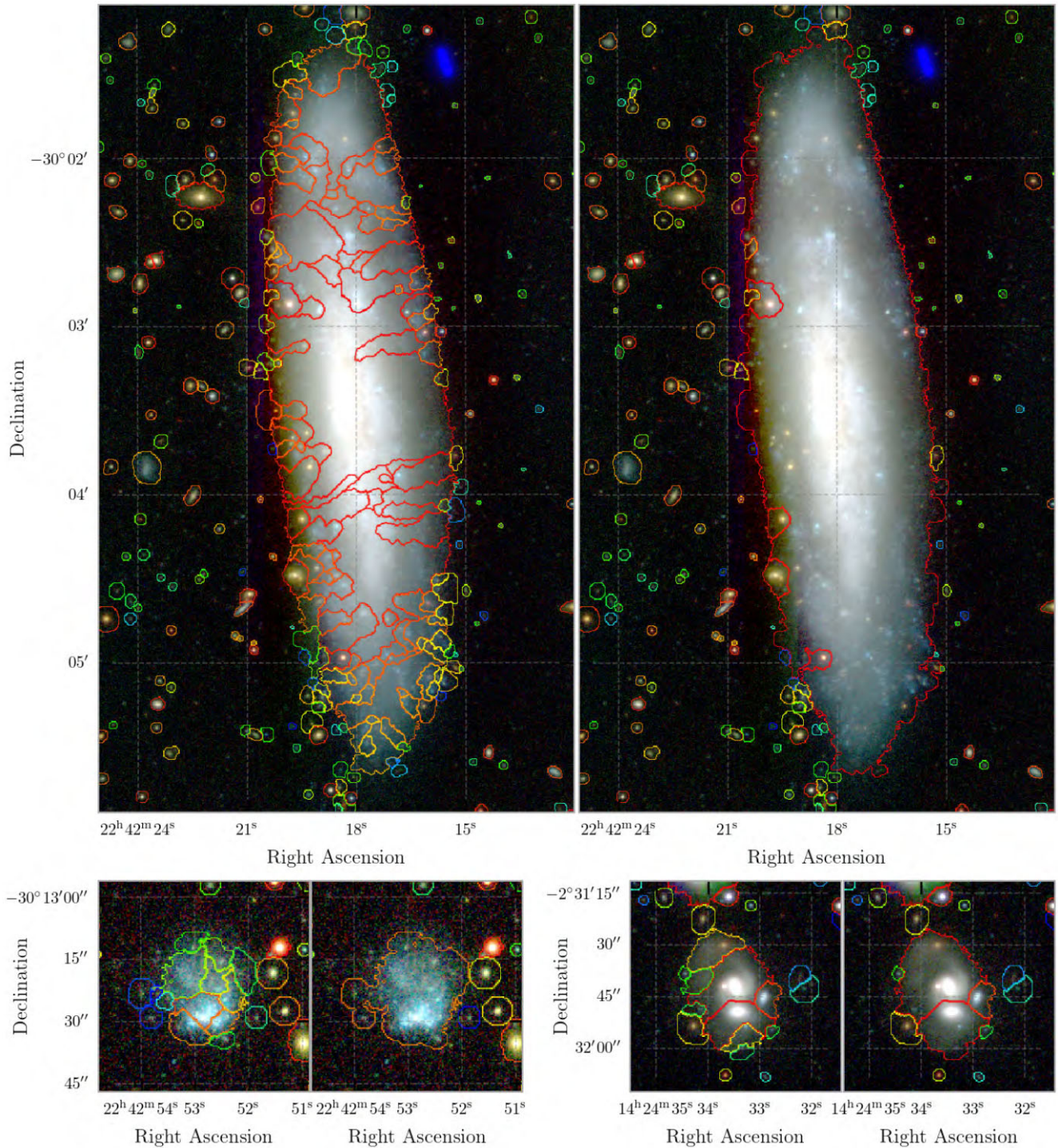


Figure 5. Three examples of objects whose segments have been regrouped using the `proFoundSegimFix` function within PROFOUND. Note how the severity of fragmentation in these examples varies. For each example, the left-hand panel plot shows the initial segmentation, whereas the right-hand panel shows the fixed segmentation.

that match back to two or more GAMA targets, corresponding to ~ 3 per cent of the total sample. As a result, an additional 44 782 GAMA targets do not appear in the KiDS/VIKING catalogues. For those cases, where multiple GAMA targets in a single PROFOUND segment had redshifts, we find that in 69 per cent of cases have $\Delta z < 0.01$, implying that in the majority of cases where GAMA targets have been consolidated, these do in fact belong to a single

object along the line of sight. This highlights that the original GAMA target catalogue had fragmented objects more often than PROFOUND has merged multiple objects into a single segment. Hence, a total of ~ 4 per cent of the GAMA target objects do not appear in our updated catalogues.

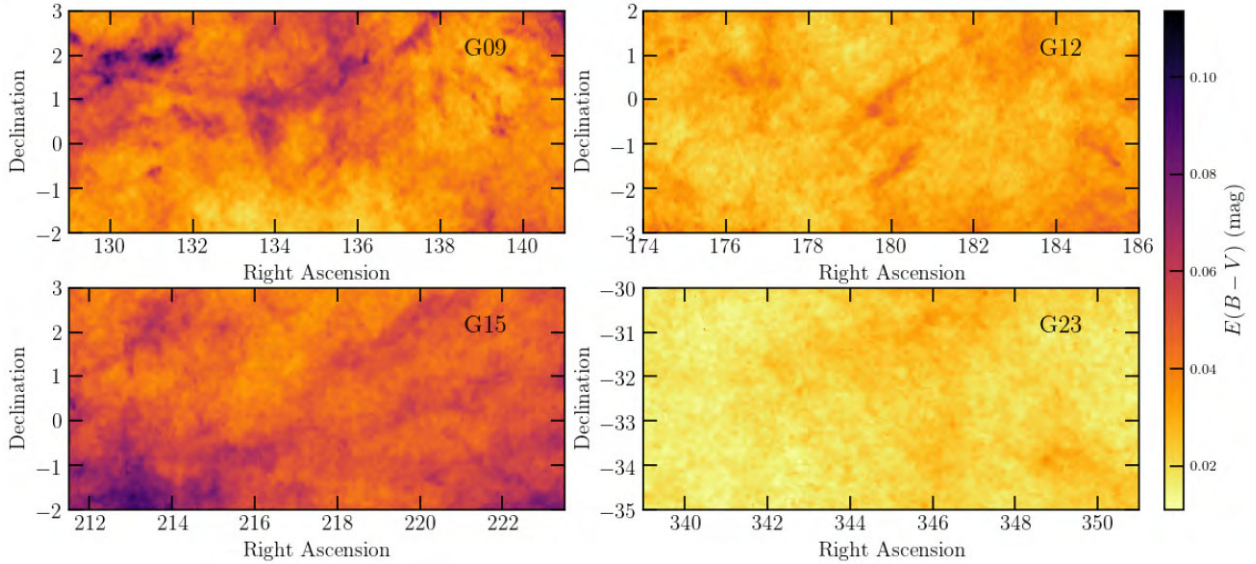


Figure 6. Galactic extinction, based on the *Planck* $E(B - V)$ values, in the four GAMA fields, clockwise from top left-hand panel are G09, G12, G23, and G15. The G23 field has the lowest extinction.

2.7 Extinction corrections using *Planck* $E(B - V)$ maps

To correct our magnitudes for the effects of Galactic extinction, we use the *Planck* $E(B - V)$ map²³ (Planck Collaboration IX 2013). From this map, we extract the $E(B - V)$ values, and convert the HEALPIX values to RA and Dec., and identify the closest $E(B - V)$ value to each object in each of our catalogues. We then correct all magnitudes, magnitude errors, surface brightnesses, surface brightness errors, fluxes, and flux-errors for *all* objects (i.e. stars, galaxies, artefacts, etc.). We determine the attenuation correction for each band in the normal way ($A_x = [A_x/E(B - V)] \times E(B - V)$) using the extinction coefficients listed and cited in Table 2 (which implicitly use the Galactic extinction law from Schlafly & Finkbeiner 2011).

Fig. 6 shows how the $E(B - V)$ values vary across the four GAMA fields highlighting the significant structure due to streaks of Galactic cirrus. However, we note the maximum $E(B - V)$ shown in the plots reaches only to 0.07, hence amounting to 0.2 mag of extinction in the r band.

2.8 Constructing the star-mask from GAIA DR2

Figs 2–4 highlight the issue of ghosting around bright stars, and how the location of this ghosting is dependent on both the position within the focal plane, and the flux of these stars. Photometry of objects in these regions will be compromised, and for many purposes it will be necessary, or desirable, for these objects to be removed. To build a star-mask flag, we elect to use the recently released GAIA DR2 catalogue (Gaia Collaboration et al. 2018), which contains robust positions for all bright objects across the sky. However, first we need to remove any galaxies in the GAIA DR2 catalogue, as we do not wish to mask these objects. To do this, we match to both the RC3 catalogue, and also our previous GAMA catalogue, which has been extensively visually inspected and for which most objects (98 per cent), have had redshifts measured to $r < 19.8$ mag (or redshifts measured out

Table 2. Attenuation values used here in conjunction with *Planck* $E(B - V)$ values to determine extinction corrections for each line of sight and in each filter. Median A_x values are determined by convolving the nearby galaxy templates from Brown et al. (2014) with the filter response curves, and assuming either a Cardelli, Clayton & Mathis (1989) ($FUV - K_s$) or Fitzpatrick (1999) (*WISE*) Galactic Extinction Law with $R_v = 3.1$.

Filter (x)	$[A_x/E(B - V)]$	Vega to AB
<i>GALEX</i>		
<i>FUV</i>	8.241 52	–
<i>NUV</i>	8.207 33	–
ESO VST Omegacam ^a		
<i>u</i>	4.811 39	–
<i>g</i>	3.664 69	–
<i>r</i>	2.654 60	–
<i>i</i>	2.074 72	–
ESO VISTA VIRcam ^b		
<i>Z</i>	1.552 22	0.502
<i>Y</i>	1.212 91	0.600
<i>J</i>	0.876 24	0.916
<i>H</i>	0.565 80	1.366
<i>K_s</i>	0.368 88	1.827
<i>WISE</i>		
<i>W1</i>	0.201 24	–
<i>W2</i>	0.139 77	–
<i>W3</i>	0.054 33	–
<i>W4</i>	0.027 20	–

^aKuijken et al. (2019).

^bGonzález-Fernández et al. (2018).

to $r < 19.2$ mag in the case of G23). Matching GAIA DR2 to RC3 results in 54 matches within the GAMA regions, while matching to GAMA identifies a further 684 objects to GAIA DR2 $g < 18.0$ mag. These are removed from our GAIA star-mask catalogue. We then extract cutouts of a random sample of GAIA stars and identify a g mag–radius relation, as shown in Fig. 7. Inside the radius indicated

²³HFI_COMP_MAP_THERMALDUSTMODEL_2048_R1.20.FITS, https://irsa.ipac.caltech.edu/data/Planck/release_1/all-sky-maps/previews/HFI_CompMap_ThermalDustModel_2048_R1.20/index.html

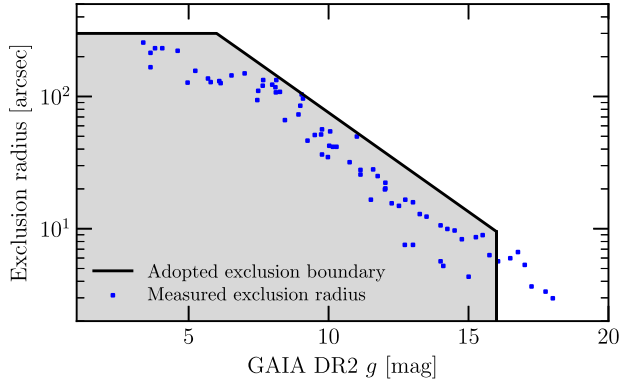


Figure 7. The star-mask exclusion radius (solid black line) was determined from eyeball measurements of randomly selected stars (blue data points) drawn from the four GAMA regions.

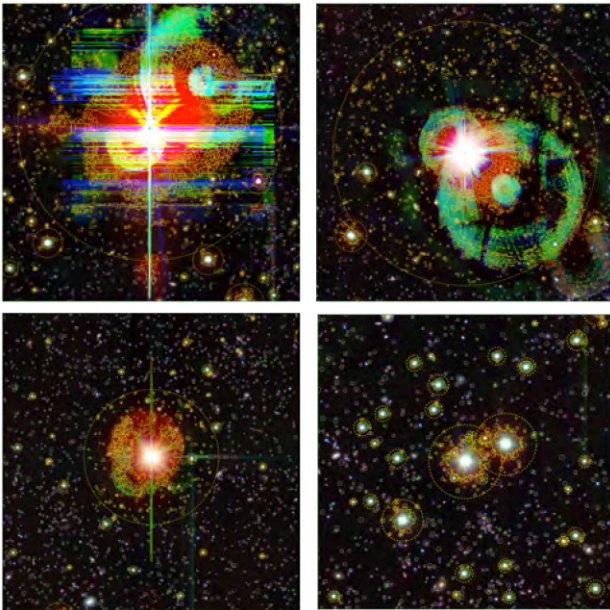


Figure 8. Four panels showing our star-mask regions, as indicated by the dotted lines. These lines are defined by equation (1). Objects within the starmask have their STARMASK flag set to 1 and are shown with yellow contours. Upper are two of our brightest stars with $g_{\text{GAIA DR2}}$ mag = 6.6 (left-hand panel) and 8.0 mag (right-hand panel). The lower panels show two more typical regions centred on stars with $g_{\text{GAIA DR2}} = 9$ th mag (left-hand panel) and 11th mag (right-hand panel) but also showing stars extending to our cutout limit of $g_{\text{GAIA DR2}} = 16$ th mag.

(solid black line), the artefact rate is extremely high, and photometry will be compromised and classification problematic.

Fig. 8 shows examples for four regions centred on four stars, showing first two extremely bright stars (which are relatively rare: upper), to two more typical regions with a smattering of masked stars (lower). The dotted circles indicate the masked region indicated by equation (1), and all objects within these regions have their STARMASK flag set to 1 and are shown on these figures with yellow outlines.

$$r[\text{arcmin}] = 10^{(1.6-0.15g)} \text{ and } [r < 5.0 \text{ arcmin}, g < 16.0]. \quad (1)$$

Note that we only define a starmask around stars brighter than 16th mag, as below this the ghosting appears to lie below the

sky noise. Fig. 8 highlights the exclusion zones around stars of various magnitudes (as indicated by the yellow segments). One can see that by 16th magnitude there is no need for exclusion regions. Fig 12 (centre panel) shows objects with STARMASK = 1 in blue, highlighting the foreground coverage lost due to bright stars. To determine the reduction in area, we create a grid of equally spaced points at 6-arcsec intervals and apply our starmask criteria. We sum the grid-points within our GAMA boundary for which STARMASK = 0. This results in the areas as indicated in Table 3.

2.9 Object classification

2.9.1 Star, galaxy, and ambiguous classification

Star–galaxy classification is performed in an initial phase using measured parameters, and then classifications are later overridden in a series of steps given prior knowledge (e.g. a known redshift, or direct eyeball classification).

In the first round, all objects are assigned a CLASS flag that is initially set to ambiguous, and therefore those objects not reclassified in the latter stages will retain an ambiguous flag.

We initially plot $(J - K_s)$ versus r_t and $\log R_{50}$ versus r_t where J and K_s are the extinction-corrected colour measurements, r_t is the extinction-corrected total r -band magnitude, and R_{50} is the effective half-light radius of the dilated segment. The latter is determined from the number of pixels within the segment. We then draw two lines on each plot to define the galaxy regions, stellar regions, and the ambiguous regions (see the solid lines in Fig. 9 that divide the data into three regions). If an object is the same class in both planes, then this class is adopted. If it is ambiguous in only one plane, then it gains the galaxy/star class, and if it is a star in one plane and a galaxy in the other, then it gains the ambiguous class. The equations used to separate the parameter spaces in the $(J - K_s)$ versus r_t space are given by

$$\begin{aligned} (J - K_s) &= 0.025, & \text{if } r_t < 19.5, \\ (J - K_s) &= 0.025 + 0.025(r_t - 19.5), & \text{if } r_t > 19.5, \\ (J - K_s) &= 0.025 - 0.1(r_t - 19.5)^2, & \text{if } r_t > 19.5, \end{aligned} \quad (2)$$

and in the $\log(R_{50})$ versus r_t space, they are given by

$$\begin{aligned} \log(R_{50}) &= \Gamma + 0.05 - 0.075(r_t - 20.5), & \text{any } r_t, \\ \log(R_{50}) &= \Gamma + 0.05, & \text{if } r_t > 20.5, \end{aligned} \quad (3)$$

where Γ is the median LOG10SEEING value.

Finally, based on the match to the GAMA redshift catalogue, we reassign any object with a confidently ($N_Q > 2$) measured redshift above 0.002 to have a CLASS flag of galaxy, and any object with a quality measured redshift of $-0.002 < z < 0.002$ to have a CLASS flag set to star.

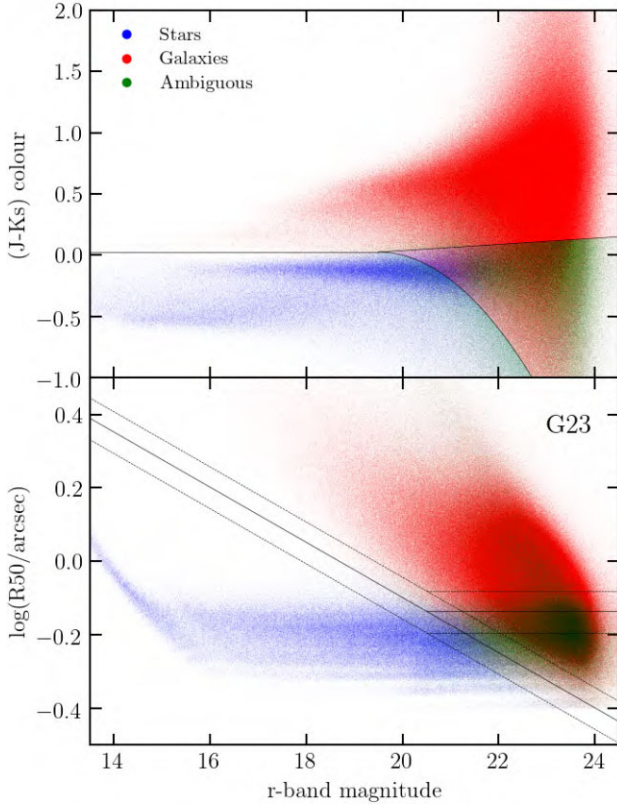
The process hence starts with ambiguity and refines the classifications through a staged process using colour and size, then redshifts. Fig. 9 shows the detected objects in the G23 region, coloured by their final CLASS flag as indicated. Note that ambiguous objects are by definition those which reside in both the ill-defined regions, unless a redshift is known or the object has been visually inspected.

2.9.2 Cleaning spurious detections

As with any data set the VST and VISTA imaging contains a variety of spurious detection issues, with origins varying from diffraction spikes and offset ghosts, to baffling issues, noisy stacks, stack edge effects, transient objects (including Mars in one frame), and satellite

Table 3. Locations of the four primary GAMA fields, their complete area coverage on the sky and the reduced are after subtracting of the area lost to the star-mask, and their astrometric offsets with respect to GAIA DR2.

GAMA field	RA range (°)	Dec. range (°)	Full area (deg ²)	Eff. area (deg ²)	Masked area (deg ²)	ΔRA (GAMA–GAIA) (arcsec)	$\Delta Dec.$ (GAMA–GAIA) (arcsec)
G09	129.0–141.0	−2 to +3	59.97	54.93	4.91	0.056	0.066
G12	174.0–186.0	−3 to +2	59.97	57.44	2.39	0.134	0.106
G15	211.5–223.5	−2 to +3	59.97	56.93	2.90	0.101	0.098
G23	339.0–351.0	−35 to −30	50.58	48.24	2.28	−0.113	0.134

**Figure 9.** Star–galaxy separation for the G23 field showing $(J - K_s)$ colour versus magnitude (upper panel), and the measure half-light radius versus magnitude (lower panel) showing the stars, galaxies, and ambiguous objects (in blue, red, and green respectively). The solid lines denote the various cuts imposed (see the text for full explanation), and the dashed lines show how these vary with seeing, with the 0.05–0.95 quantile range of the LOG10SEEING value shown.

trails, etc. To identify artefacts, we use a series of cuts to highlight objects in improbable parameter space. These have been arrived at through fairly extensive testing and visual checking and, in particular, viewing bright objects for which no match exists in the GAMA catalogue. From this process, we arrive at a series of diagnostic flags and cuts as indicated in Table 4. Note that the table is progressed from the top to bottom allowing overrides, hence we move from less certain to more certain classification markers. Fig. 10 shows a single deg² for a problematic region indicating some of the issues: bright star ghosting, baffling issues, missing data, offset ghosting, and frame edge effects. Overlain are objects with STARMASK flag set (orange), class set to artefact (cyan), and some remaining objects with bright fluxes not previously detected in the SDSS GAMA catalogue (purple). About half of the objects in this latter category represent new objects. An example of the object classifications is shown in

Fig. 11, where the segment of each object in this field is coloured by the corresponding classification, as indicated in the caption. The process is never going to be perfect but we believe the unclassified artefact rate is now well below 1 per cent of the galaxy population. We also note that no objects are removed and hence alternative or additional cleaning can be applied as we improve our understanding of the data.

2.10 Merging the PROFOUND catalogues

Having generated 280 independent deg² tiles across the four GAMA fields, we now need to combine these into four catalogues (one for each GAMA region), by merging while removing duplicates in the overlap regions. Fig. 12 highlights the issue by showing the concatenated TILE catalogues without consideration of duplicates. The overdensity of the overlap regions manifests as a regular tartan-like pattern representing the double detection of objects in these regions. A simple coordinate match in the overlapping regions is insufficient to identify duplicates, as there are a number of reasons why the two sets of coordinates may not be identical:

- (i) An object in the overlapping region may have been visually regrouped in two slightly different ways. If so, some segments may exist in one field, but not the other.
- (ii) Very noisy segments, due to slightly different PROFOUND sky solutions, may have different boundaries and hence different coordinates.
- (iii) Segments that include multiple sources (which can occur if the saddle point between sources falls above the CLIPTOL threshold) may also have different RAMAX and DECMAX values²⁴ if the sky solutions differ slightly.

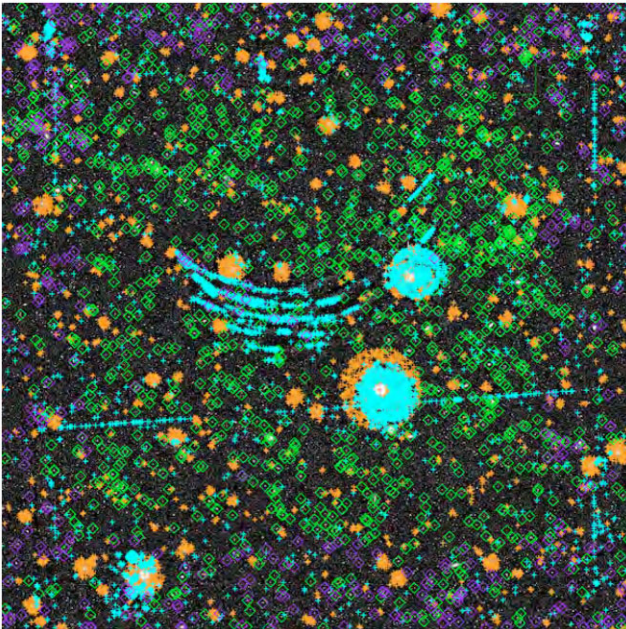
In all three of the above scenarios, a simple coordinate match will not identify ‘lone’ objects that have not been exactly duplicated, and these objects will be counted twice. The following measures have been taken to account for these scenarios:

- (i) A check for duplicate objects is conducted exclusively in the overlapping regions. In these regions, any object that is *not* duplicated is immediately assumed to be spurious, and is assigned `DUPLICATE = 1`. In the scenario of differently merged objects, this ensures that only the ‘main’ segment of the galaxy will be considered. Additionally, all noisy segments without stable coordinates will be given `DUPLICATE = 1`.
- (ii) For each successfully duplicated object, priority is given to the duplicate with more flux. In the scenario of differently merged objects, this ensures that only the most aggressively regrouped

²⁴For each object, PROFOUND computes two sets of coordinates. RAMAX/DECMAX values indicate the coordinate of the brightest pixel within a segment, whereas RACEN/DECEN values show the flux-weighted central coordinate of the segment.

Table 4. A summary of the diagnostic markers, note diagnostics higher in the table supercede those lower down, hence the table also represents a priority when updating the same flag.

Flag	Default	Setting	Criteria	Reason
Class	Ambiguous	Galaxy	GAMA match with $Z > 0.002 \& NQ > 2$	Known GAMA galaxy
Class	Ambiguous	Star	GAMA match with $-0.002Z < 0.002 \& NQ > 2$	Known GAMA star
Class	Ambiguous	Artefact	$(m_{\text{rt}} - m_{\text{Z}}) < -0.75$	Improbable $(r - Z)$ colour
Class	Ambiguous	Artefact	$\log_{10}(R50) < -0.4$	objects size is smaller than one pixel
Class	Ambiguous	Artefact	No detection in two of gri bands but optical data exists	Only detected in 1 optical band
Class	Ambiguous	Artefact	No detection in three of $ZYJHK_s$ bands but NIR data exists	Only detected in 1 or 2 NIR bands
Class	Ambiguous	Artefact	$\sigma_{\text{RMS}} > \text{median}(\sigma_{\text{RMS}}) - 5 \times \text{st.dev.}(\sigma_{\text{RMS}})$	Elevated skynoise
Class	Ambiguous	Star	$\text{starsize} + \text{starscol} > 3.5$	Star
Class	Ambiguous	Galaxy	$\text{starsize} + \text{starscol} < 0.5$	Galaxy
Starmask	0	1	$r(\text{arcmin}) = 10^{(1.6 - 0.15g)}$ and $(r < 5.0 \text{ arcmin}, g < 18.0)$	Object lies near a bright GAIA DR2 star
Duplicate	0	1	Does not appear in all overlapping regions	Any object that has not been detected in all overlapping square degrees is spurious.
Duplicate	0	1	Duplicate identified by coordinate match with either cen or max coordinates, flag is assigned to the object with less flux	Segment is incomplete, either due to frame edge, or insufficient segment rebuilding.
Mask	0	1	RA, Dec.	Inside the GAMA footprint
Z_confusionFlag	0	1	Δz of multiple GAMA target matches > 0.1	Segment contains flux from multiple GAMA objects at different redshifts.

**Figure 10.** Problematic deg^2 region showing many of the issues we face. Overlain on the image are objects within starmask regions (orange) and objects labelled as artefacts (pale blue). Other objects that are bright but have no known GAMA counterpart are shown in purple. Finally, known GAMA galaxies are shown in green.

version of an object will have $\text{DUPLICATE} = 0$. Additionally, if objects have been broken up due to proximity with the edge of the tile, then the version of the object that is most complete will be prioritized.

(iii) In the overlapping regions, a duplication is checked for with both the RAMAX/DECMAX coordinates, and also the RACEN/DECCEN coordinates. If an object is flagged as being a duplicate in either one, then it will be assigned a value of $\text{DUPLICATE} = 1$. This has been done because even if a stable segment has differing RAMAX/DECMAX values due to a slightly different sky solution, the RACEN/DECCEN values tend to be the same. As such, segments whose brightest pixel position fluctuate due to different sky solutions are adequately accounted for.

Hence, $\text{DUPLICATE} = 0$ will produce a catalogue of unique objects, whereas $\text{DUPLICATE} = 1$ will produce a catalogue of redundant objects (see the blue-grey bands in the centre panel of Fig 12). Note that no objects are removed from the catalogue at any stage, instead we introduce flags to enable extraction of well-defined samples.

3 EXTRACTING PHOTOMETRY IN THE MID-INFRARED (MIR) AND FIR

Objects in the MIR–FIR are unresolved, unlike the FUV–MIR bands where objects are either fully or partially resolved. In addition, some of the brightest far-IR sources may have no or minimal optical fluxes, and vice versa. Finally, the depth of the FIR imaging is also lower than optical images (as shown in Fig. 18). We therefore run PROFUND in a manner that utilizes a different measurement technique in the MIR–FIR. To account for the above differences between the MIR–FIR and FUV–MIR, the FIR fluxes of optically identified objects are iterated over by applying expectation maximization (EM), as we describe in the following section.

The philosophy of this measurement approach is to model the FIR flux of each optically detected object, and then iterate over the flux of the object in each band, ensuring that all FIR flux is accounted for. In each band separately, the locations of optically selected objects provide the coordinates at which to fit for objects. For the W3–W4 bands, the input objects are selected to be all objects from the optical catalogue with $m_r < 20.5$ mag, excluding those objects with an $\text{UBERCLASS} = \text{artefact}$ flag. Because stars are still bright at these wavelengths, we make sure to model their flux contribution. In the $P100$ – $S500$ bands, however, we also remove all objects with $\text{UBERCLASS} = \text{star}$ or ambiguous flag, as these objects are not expected to emit FIR flux. A magnitude guess for each object is determined by running an initial round of PROFUND at the input coordinates. Based on this initial magnitude guess, PROFIT²⁵ (Robotham et al. 2017) is applied to construct a model of each object given the PSF of each band and the magnitude guess of each object, to create a model of the FIR-emitting sources within the tile. This PROFIT model is then subtracted from the image to produce a residual image. Iteratively, the model fluxes are modified using EM in order to minimize the flux remaining in the residual image. After these initial iterations, any additional FIR-emitting sources that are

²⁵ Available on Github: <https://github.com/ICRAR/ProFit>

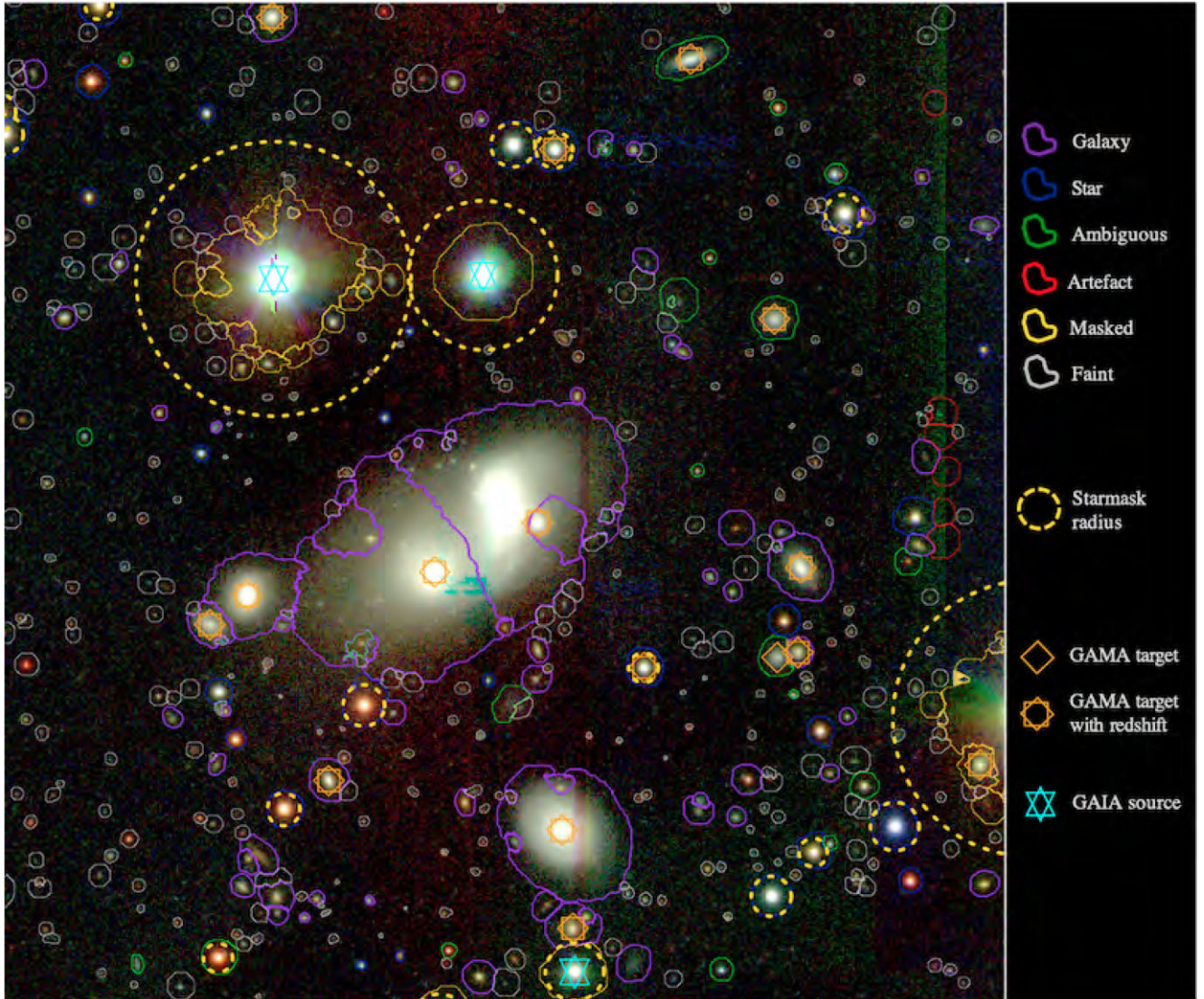


Figure 11. An example 6×6 arcmin² region showing the final classifications as described in the text: galaxies with $Z < 21.5$ mag (purple), stars with $Z < 21.5$ mag (blue), ambiguous with $Z < 21.5$ mag (green), artefacts (red), faint (grey), and masked (yellow). For masked stars, the starmask region is shown with a dashed yellow circle. GAMA targets are shown as orange diamonds, and GAIA sources are indicated with cyan stars. The region shows a number of complexes where the watershed deblending technique (by which every pixel is assigned to a single object only) is apparent.

not present in the original optical catalogue will be apparent. These are now identified using PROFOUND in source detection mode, and are included from this point onwards in the analysis as ‘additional sources’. The inclusion of these additional sources mainly serves the purpose of accurate flux determination, to ensure that no background FIR flux is attributed to a foreground catalogue object.²⁶ Once a catalogue of both optically selected and additional sources has been determined, PROFOUND is run over the full image to determine the magnitudes of all objects, again in an iterative sense. Some of these objects will be marginalized out by PROFOUND, producing very low

²⁶Note that if a background source exists within the PSF of the foreground object, then this flux will no longer be separated. Such a scenario was presented by Allison et al. (submitted), where the SED of the target foreground object was likely polluted in the FIR through the contribution of a high- z background object.

flux values, with correspondingly large uncertainties. This process is conducted using the `profoundFitMagPSF` command, which we show for completeness in the Appendix.

To account for potential oversubtraction of the sky in the data-reduction phase of the FIR imaging (possible due to the confused nature of sky pixels), we do an explicit sky subtraction in each band in a second phase. During the detection phase of additional sources, as described above, PROFOUND makes a measurement of the sky. In this second phase, we rerun the command as described above, in which the input image has undergone an explicit sky subtraction.

In total over the four GAMA fields, photometry was measured for 822 326 objects with an `UBERCLASS = galaxy` flag with $m_r < 20.5$ mag. The fraction of these objects with detections in each band (defining a detection as having a measured magnitude < 30) varied in each band, depending on the depth of the imaging. In the $W3/W4/P100/P160/S250/S350/S500$ bands,

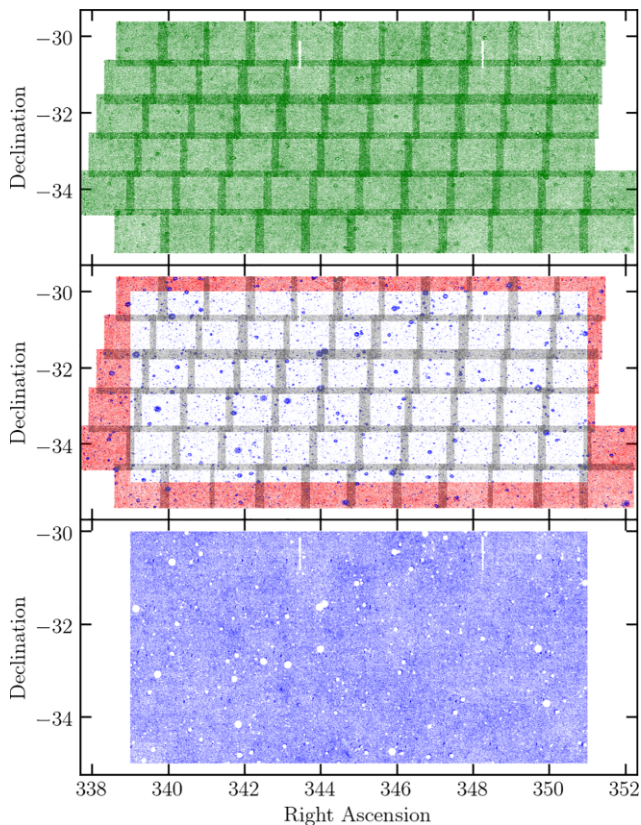


Figure 12. The progression of the data flow for the G23 field. Top panel: PROFOUND is used to process each deg^2 TILE plus overlap to generate the star plus galaxy source catalogue shown (green points). Centre panel: The GAMA boundary is applied (red) and galaxies in the overlap region identified (grey), the star-mask is then applied (blue) and regions with missing photometry are identified (cyan). Lower panel: The final galaxy catalogue (blue) showing only those galaxies in high-quality regions away from bright stars or missing data.

62/42/38/43/50/42/32 per cent of objects had detections, respectively. In total, 38 413 objects had detections in all seven bands, corresponding to just under 5 per cent of the $m_r < 20.5$ mag galaxy sample.

The resulting uncertainties, due to the EM mixture modelling process, accurately reflect the inherent uncertainties in this process. If two optically detected sources are close in projection, then the uncertainty will reflect the potential confusion between these two sources. We show in Fig. 13 an example of the original image, final modelled image, and resulting residual of a specific square degree. Note that in this example, the main features in the residual image originate from resolved galaxies that are not well modelled by the PSF. In addition to the objects detected in the FIR with optical counterparts, 4.5/43.4/0.3/0.4/23.6/19.6/4.9 per cent of objects in the W3/W4/P100/P160/S250/S350/S500 bands were identified as ‘additional sources’. Generally, this percentage is reflective of the depth of the imaging. We note that the large number of additional objects detected in the W4 band indicates that the PROFOUND parameter used to identify these objects was likely too aggressive in this band.

The above process is conducted independently for each band in each individual tile. In total, it requires less than one hour to extract the W3–S500 photometry for a single square degree. The outputs for the additional sources are saved, however, are not included in our final catalogue. An analysis of these sources is beyond the scope of this work.

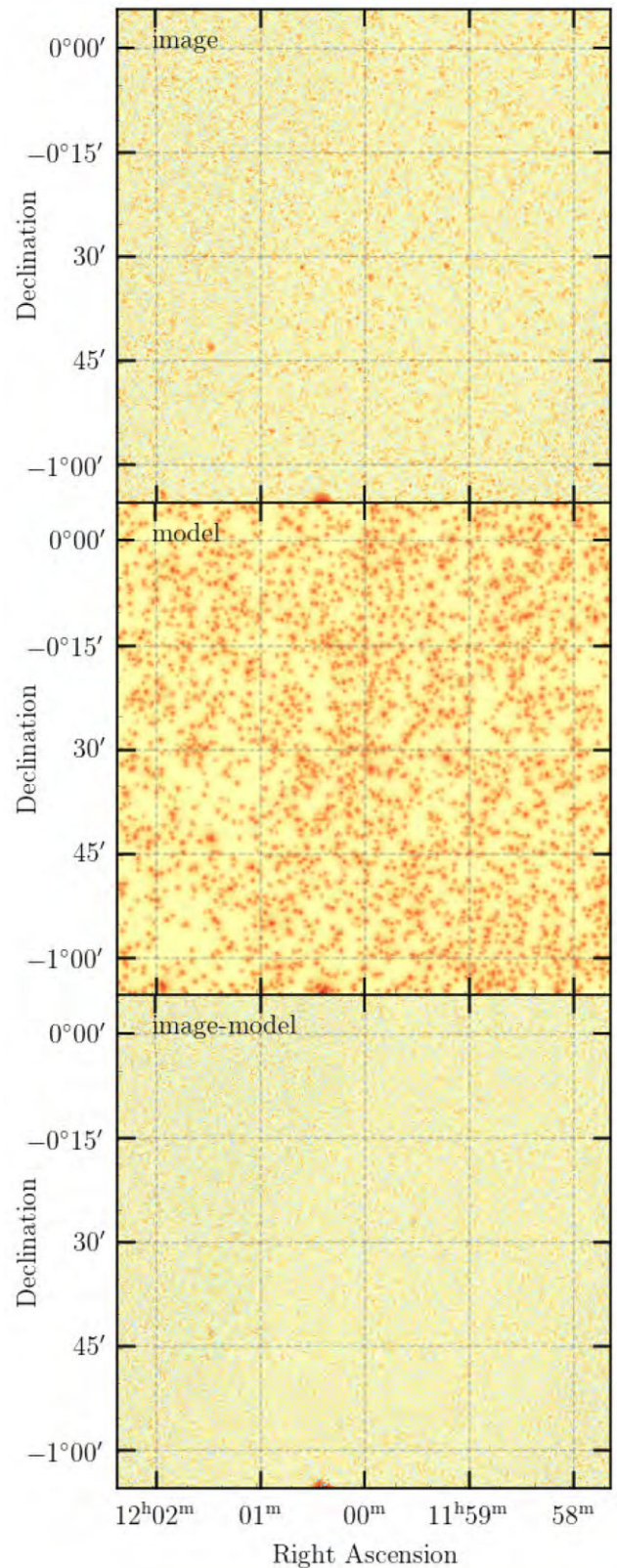


Figure 13. Example of the photometry extraction in the SPIRE 250 band for a single tile in the G09 region. The top panel shows the original image, and the middle panel shows the PROFIT-produced model of the objects. The residual when subtracting the model of the image is shown in the bottom panel.

4 VERIFICATION AND VALIDATION

4.1 Comparison with previous photometry

4.1.1 Comparison to SDSS/2MASS

Fig. 14 shows a comparison of the PROFOUND measured photometry of stars (in selected magnitude ranges) to either SDSS DR13 (*ugriz*) or 2MASS (*JHK_s*). For the comparison to SDSS in the *u* and *r* bands, we use the filter conversions as outlined by Kuijken et al. (2019). For the comparison to 2MASS, we include the appropriate corrections for the 2MASS filter shapes, colour terms, and AB to Vega corrections given in González-Fernández et al. (2018). The effect of saturation in the VST *gri* and VISTA *Z* bands is evident at the bright end, where PROFOUND recovers less flux for the bright stars than was measured by SDSS. Note that the SDSS data are *not* corrected for the known *u* and *z* offsets from the SDSS system to the AB system. In all bands, the photometry agrees well with scatter about the equality line increasing slightly towards fainter fluxes. In all cases, the offsets are <0.06 mag with the largest offset seen in the *K_s* band.

4.1.2 Comparison to LAMBDAR

We compare the colour distributions of the photometry presented in this paper against equivalent colour distributions produced by LAMBDAR (Wright et al. 2016) for the subset of objects with measured 20-band photometry, as shown in Fig. 15. The left-hand panel of the plot features the relative colour distribution of the overlapping sample between LAMBDAR and the new photometry. Blue histograms refer to the new photometry presented in this paper, whereas orange histograms refer to the LAMBDAR photometry. For each histogram, we show the 0.1–0.9 quartile range with a horizontal line, where the median value is shown. Note that the colour values have been shifted so that the peak in the distribution for the new photometry is at 0. The right-hand panel of the plot shows the number of outliers in each sample for each band, where outliers are determined to be objects that have colours more than 0.5 mag outside the 0.1–0.9 quartile range. The new colour distributions are improved in the UV, optical and also (marginally) the FIR bands, however, we note that the colour distributions in the NIR bands are better in LAMBDAR. This is likely the result of the generous segment dilation, we have implemented in order to catch halo flux, adding more sky noise than in LAMBDAR.

4.2 Seeing variations across tiles

By analysing the R50 values of stars across the four GAMA fields, we are able to determine the extent to which the seeing varies across the tiles in each of the optical/NIR bands. The median R50 value varies between ~ 0.4 and 1 arcsec over the four fields, in each of the different photometric bands. Due to the nature of the segment dilation within PROFOUND, the total flux within each object is accounted for despite potential variations in the PSF. To check that these PSF variations are not having an impact on the derived fluxes for galaxies in the sample, we assess how the minimum R100 value for galaxies compares to the PSF in each tile. For galaxies down to an *r*-band magnitude of 23, we find that the smallest galaxies are on average larger than the PSF by factors of 2–4. This confirms that galaxy segments are consistently larger than the PSF, meaning that seeing variations across the tiles are not affecting the measured fluxes of galaxies in our photometry.

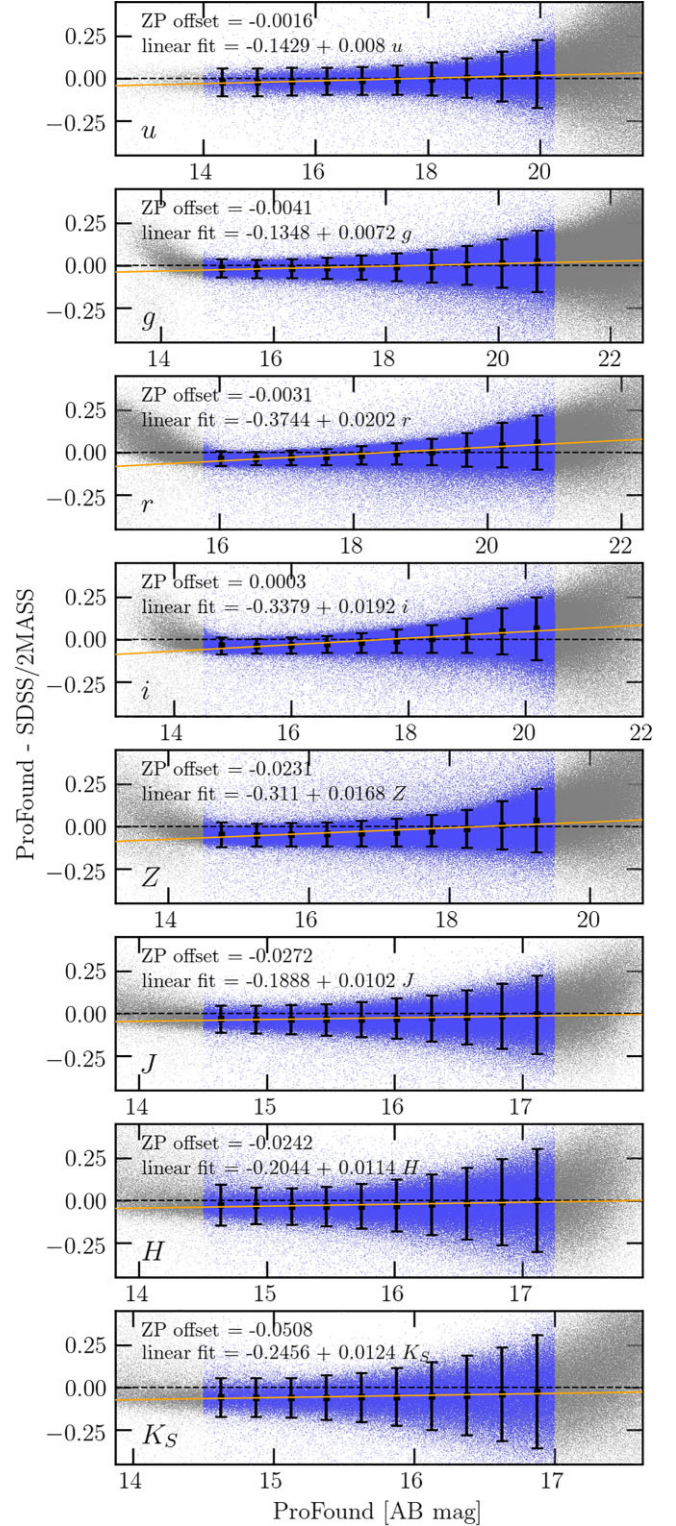


Figure 14. Comparison of the new PROFOUND photometry versus the SDSS/2MASS photometry, for the combined G09 + G12 + G15 data in the filters indicated for stars only. In each panel, we show the data (grey dots for the full sample, and blue dots within the fitted magnitude range), the median offset (black points with 1σ range), and the linear fit to the offset (orange line). The offset and the least-squares fit to the median values are shown in the upper left-hand panel of each panel.

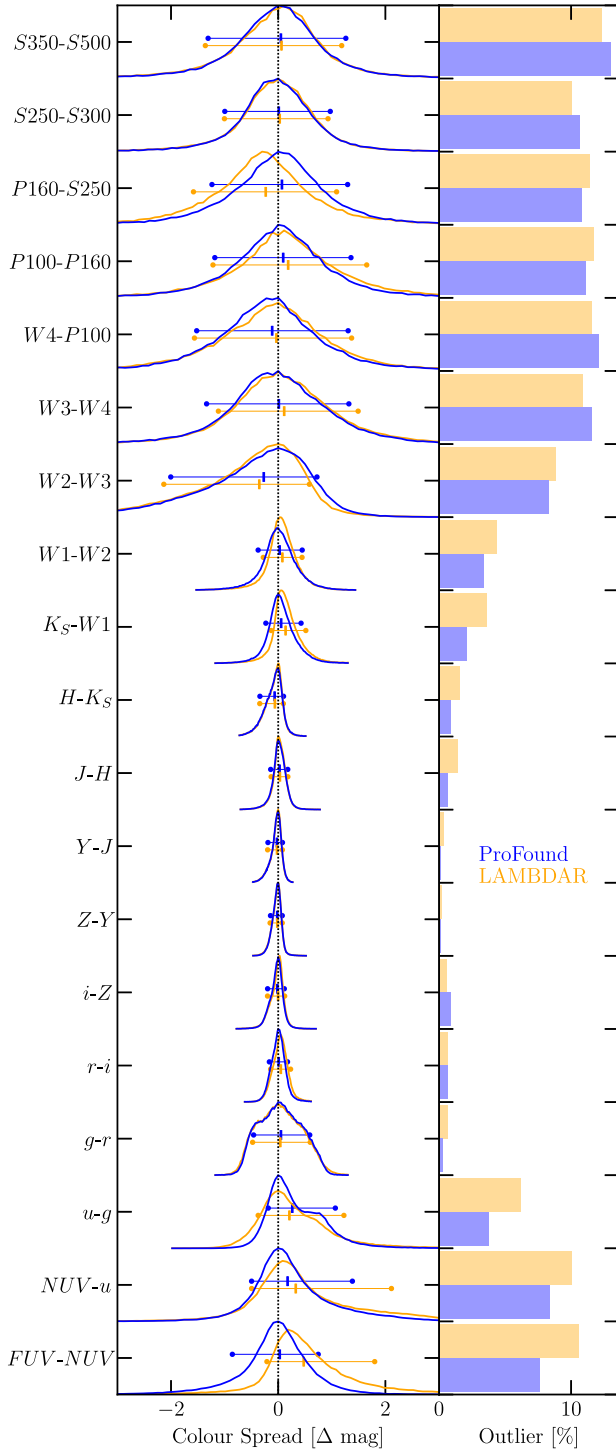


Figure 15. Colour distributions of all adjacent bands for the photometry presented in this paper (blue), as compared with LAMBDAR (Wright et al. 2016) (orange) for all matching galaxies. Individual colour distributions are shown in the left-hand panel, relative to the peak of the PROFOUND colour distribution. We show the 0.1–0.9 quantile ranges for each sample, as well as the median value. The right-hand panel shows the outlier percentage for each sample, quantified as the percentage of points that lie further than 0.5 mag away from the 0.1–0.9 quartile range.

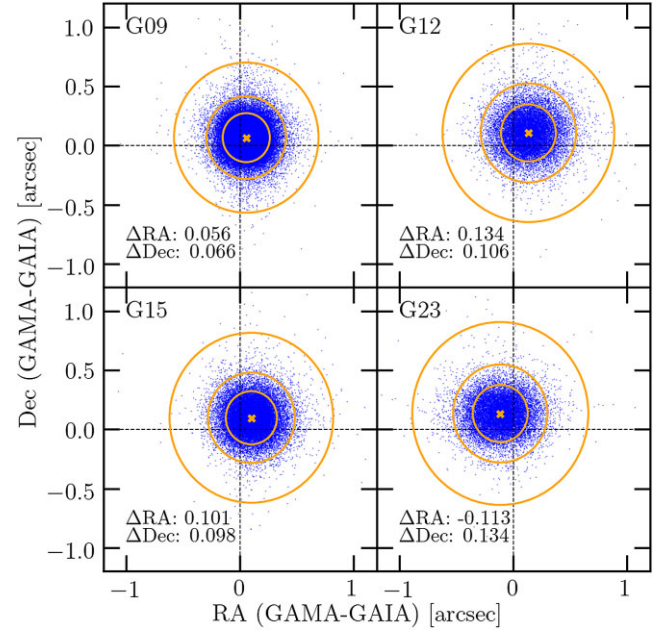


Figure 16. Astrometric accuracy of the native VST KiDS data against GAIA DR2 for each of the GAMA regions as indicated.

4.3 Final astrometric accuracy

To verify the astrometric accuracy, we identify objects selected as stars in the range $14 < m_r < 16$ and match against GAIA DR2 (Gaia Collaboration et al. 2018; Lindegren et al. 2018) taking the best match within 3 arcsec. Fig. 16 shows the RA and Dec. offset for each field, with the medians indicated (orange crosses) and the circles enclosing 1σ , 2σ , and 3σ . In all cases, the 3σ astrometry error is within ± 0.75 arcsec but some modest offset is seen. We therefore add two extra columns RAGAIA and DECAGAIA where we correct the VST KiDS astrometry to the GAIA astrometric frame by implementing a simple RA and Dec. offset appropriate to each region. The offsets are as shown in Table 3 (columns 7 and 8).

4.4 Star and galaxy counts in each region

As an initial diagnostic, we construct the galaxy number counts for each region and compare to literature data from Driver et al. (2018) in the r band (see Fig. 17). Within each panel, we show the galaxy counts (red) and the star counts (blue), where the shaded regions indicate the range covered when ambiguous objects are included. Note that the ambiguous objects are not explicitly included in either main line. Literature counts are shown in grey and the predicted star counts from the TRILEGAL v1.6 model (see Girardi et al. 2012), are shown with an orange dotted line. In all four regions, the recovered r band counts show broad agreement with the literature data. The galaxy number counts are slightly below the literature counts at the bright end in both the G09 and G23 fields. We note that the TRILEGAL models also agree well with our star count data and suggest that the majority of the ambiguous detections are likely stars (as the upper bound of the star counts most closely matches the TRILEGAL prediction), and as also suggested by Fig. 9. More details will be discussed in Koushan et al. (in preparation).

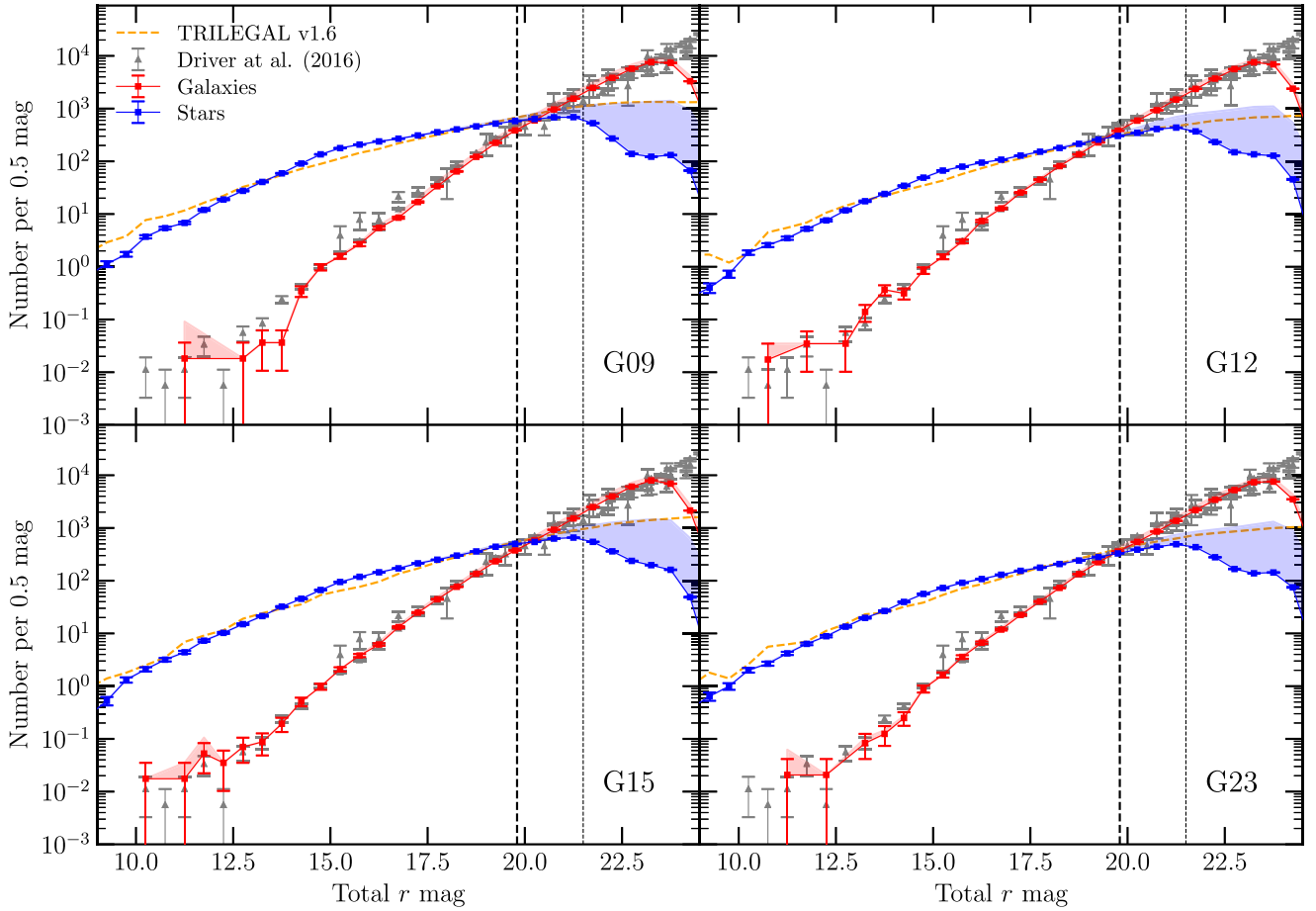


Figure 17. Galaxy and star counts for each of the four GAMA fields, as labelled. The errors are the combination of root- n statistics (shown as error bars, dominating at bright magnitudes) combined linearly with the star–galaxy classification error (shown as the coloured region, dominating at faint magnitudes). The vertical lines show the nominal GAMA spectroscopic survey limit (dashed lines) and the upcoming WAVES spectroscopic survey limit (dotted line). Data shown are taken from the compendium of Driver et al. (2016a) that combined ground-based and space-based filters through comparable, but not identical, bandpasses.

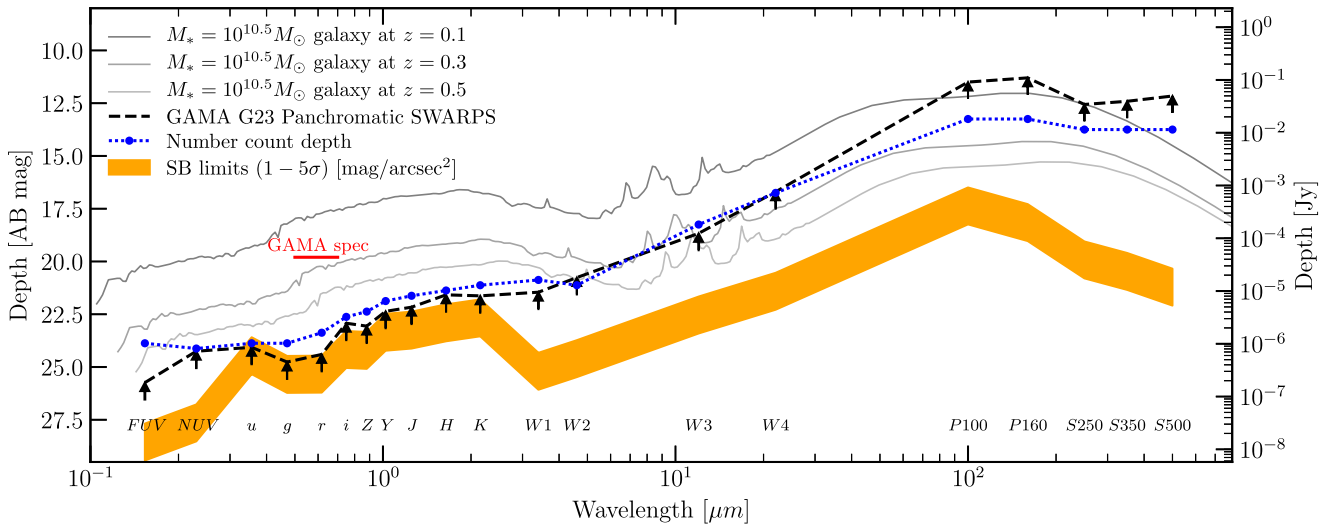


Figure 18. The revised panchromatic depth for the G23 field, now including the VST KiDS data. The stated 5σ depth levels in each of the bands is shown in black, whilst our depth measurement based on the turnover magnitude from the number counts in each band is shown as the blue dotted line. Not that this measurement is shallower in the FUV, g , r , and i bands, while being deeper in the Herschel bands. The surface brightness limit of the images as determined by the PROFUND-measured skyRMS values is shown in the yellow shaded region. The spectroscopic limit of the GAMA survey is shown in red. Template SEDs for a $M_* = 10^{10.5} M_\odot$ galaxy at varying redshifts are shown in grey. These are generated using the tool PROSPECT (Robotham et al. 2020).

4.5 Revised panchromatic depth

We show in Fig. 18 the revised depth of our imaging and catalogues in each of the 20 photometric bands. In addition to showing the stated 5σ depth limits for each of the imaging bands in black, we make two separate measurements of the depth of our data. The first utilizes the number counts of each band, as described in the above Section 4.4, to estimate the depth in each band as the magnitude at which the galaxy counts turn over (calculated as the magnitude at which the counts are lower than the counts in the previous magnitude bin). This measurement is shown in Fig. 18 as the dotted blue line. We note that this measurement is very close to the stated depths, except in the FUV, g , r , and i bands where our depth measurement is shallower, and the Herschel bands in which our measurement is deeper.

As an alternative way of indicating the image depth, we plot the surface brightness limits in each band as determined by the PROFOUND-measured skyRMS values in each band. These limits are shown in Fig. 18 as the yellow shaded region.

We compare these revised depths with a PROSPECT-generated SED for a $M_* = 10^{10.5} M_\odot$ galaxy with a constant SFH at redshifts of $z = 0.1, 0.3$, and 0.5 . This comparison highlights that, with our sensitivity, at $z = 0.3$ we are no longer sensitive to a galaxy of this stellar mass in the FIR.

4.6 Impact on existing GAMA studies

The main impact that this new catalogue will have on existing studies comes from the new segmentation maps. As discussed in Section 2.6, not all objects in previous GAMA studies will be listed in this new catalogue, as they have been merged with neighbouring GAMA objects, or because the target was based on an artefact in SDSS imaging. This is the case for ~ 4 percent of GAMA targets. As a test of the impact of this on existing GAMA studies, we assess the number of objects in existing data products that no longer appear in the new catalogue. In the catalogue of visual morphologies (DMU *VisualMorphologyv3* Kelvin et al. 2014a, as used in, for example, Kelvin et al. 2014b; Alpaslan et al. 2015; Lange et al. 2016; Moffett et al. 2016a, 2016b), 0.81 percent of objects are not in the new catalogue. For the group catalogue (DMU *G3Galv10* Robotham et al. 2011, as used in, for example, Alpaslan et al. 2012; Lara-López et al. 2013; Alpaslan et al. 2014; Robotham et al. 2014; Davies et al. 2015; Deeley et al. 2017), this number is only 0.26 percent. For the SED-fitting catalogue using MAGPHYS (DMU *MagPhysv06* Driver et al. 2016c, as used in, for example, Davies et al. 2017; Driver et al. 2018; Mahajan et al. 2018) only 0.25 percent of objects are missing, and for the catalogue of Sérsic indices (DMU *SersicCatSDSSv09* Kelvin et al. 2012, as used in, for example, Kelvin et al. 2014a; Deeley et al. 2017; Bremer et al. 2018) 0.87 percent of objects are missing. This corresponds to an absolute number of 314/470/487/1935 galaxies respectively. We highlight that this number is very small, and hence do not expect that this will have any impact on existing GAMA studies. The GAMAKIDSVIKINGCATAIDMATCHV01 catalogue will aid in the bookkeeping of any such circumstances, by identifying for each GAMA target the corresponding UBERID in the new catalogue.

5 ACCESS TO CATALOGUES

The catalogues are available to any member of the public via a collaboration request.²⁷ Included in the release are the data management units (DMUs) as described in Table 5.

Each of these includes DMU descriptions in the GAMA Schema Browser and tools to access the data via either the Single Object Viewer (Liske et al. 2015) or the Panchromatic SWARP Imager (Driver et al. 2016c). Note that the spectroscopic component is described in full in Liske et al. (2015). Note that version numbers may change as products are updated, however, older versions are available via the Schema Browser.

5.1 Usage of DMUs

In the analysis described within this paper, we have kept all measurements and introduced a series of flags (see Table 4) to indicate various issues. Hence, the extraction of a catalogue suitable for science requires the use of these flags. For example, to extract all galaxies in the GAMA G09 region outside the starmask with robust spectroscopic redshifts from the KIDSVIKINGGAMAV01 catalogue one must execute the following:

```
uberclass='galaxy' & duplicate=0 &
mask=0 & starmask=0 & region='G09' & NQ >
2
```

This results in 59930 galaxies covering 54.93 deg^2 of sky (see Table 3).

The FIR catalogue (KIDSVIKINGGAMAFIRv01) only includes a subset of the objects in KIDSVIKINGGAMAV01, as per the description in Section 3. In all other respects, however, the structure of the catalogue is the same. The same set of flags to isolate catalogues has been implemented. Conducting the above command on this catalogue hence results in 58967 galaxies covering 54.93 deg^2 of sky (see Table 3).

6 SUMMARY

We present in this paper updated photometry of four GAMA fields in 20 wavelength bands, using deeper imaging from KiDS/VIKING and the code PROFOUND. PROFOUND has been separately run in first a resolved mode to extract photometry from first the FUV–W2 bands, and then in an unresolved to extract photometric measurements from the W3–S500 bands. In the resolved mode, sources are detected, fragmented sources are visually rebuilt, and then the corresponding fluxes in all bands are extracted, before correcting these values for dust extinction, defining starmasks, and classifying the individual objects into classes of star, galaxy, or ambiguous. Spurious objects in the catalogue are assigned the class of artefact. The photometry in the unresolved regime is conducted using a subset of the resolved catalogue as an input, where fluxes are extracted in an expectation maximisation manner for objects that are identified as galaxies with $m_r < 20.5$. As part of this process, we identify additional sources that contribute flux in each FIR band (most probably background sources), however, we leave an analysis of these objects to future work.

As a verification of the new photometry, we have checked the astrometry of stars in our catalogue against their coordinates in GAIA, to identify our astrometric accuracy. A comparison of the galaxy and star number counts to literature data from Driver et al. (2016c) show that our galaxy number counts are consistent with the literature in all fields, with only a slightly smaller count number at the bright end in the G09 and G23 fields. We identify that the colour distributions in our new photometry, as compared with the previous LAMBDA photometry (Wright et al. 2016), are significantly tighter in the UV and optical bands, and also marginally better in the FIR bands.

²⁷<http://www.gama-survey.org/collaborate/>

Table 5. DMUs released as part of this paper.

DMU	Description
GAMAKidsVikingv01	PROFOUND FUV–NIR analysis described here
GAMAKidsVikingCATAIDMatchv01	CATAID match of legacy catalogues to new catalogue
GAMAKidsVikingFIRv01	PROFOUND FIR PSF-limited analysis described here
GAIADR2GAMAstarmaskv01	List of GAIA DR2 stars that define the starmask

In future work (Bellstedt et al. submitted), this photometry will be used to conduct SED fitting with the newly developed code PROSPECT (Robotham et al. 2020) to measure stellar masses, star formation rates and star formation histories for individual galaxies.

ACKNOWLEDGEMENTS

We thank the anonymous referee for their careful reading of this work, and whose comments improved the paper. SPD and SB acknowledge support from the Australian Research Council under Discovery Project Discovery 180103740.

GAMA is a joint European–Australasian project based around a spectroscopic campaign using the Anglo-Australian Telescope. The GAMA input catalogue is based on data taken from the SDSS and the UKIRT Infrared Deep Sky Survey. Complementary imaging of the GAMA regions is being obtained by a number of independent survey programmes including *GALEX* MIS, VST KiDS, VISTA VIKING, *WISE*, Herschel-ATLAS, GMRT, and ASKAP providing UV to radio coverage. GAMA is funded by the STFC (UK), the ARC (Australia), the AAO, and the participating institutions. The GAMA website is <http://www.gama-survey.org/>. This work is based on based on observations made with ESO Telescopes at the La Silla Paranal Observatory under programme IDs 177.A-3016, 177.A-3017, 177.A-3018, and 179.A-2004, and on data products produced by the KiDS consortium. The KiDS production team acknowledges support from: Deutsche Forschungsgemeinschaft, ERC, NOVA and NWO-M grants; Target; the University of Padova, and the University Federico II (Naples).

This work was supported by resources provided by the Pawsey Supercomputing Centre with funding from the Australian Government and the Government of Western Australia. We have used R (R Core Team 2017) and PYTHON for our data analysis, and acknowledge the use of MATPLOTLIB (Hunter 2007) for the generation of plots in this paper.

REFERENCES

Allison J. R. et al., 2020, *MNRAS*, 494, 3627
 Alpaslan M. et al., 2012, *MNRAS*, 426, 2832
 Alpaslan M. et al., 2014, *MNRAS*, 440, L106
 Alpaslan M. et al., 2015, *MNRAS*, 451, 3249
 Andrews S. K., Driver S. P., Davies L. J. M., Kafle P. R., Robotham A. S. G., Wright A. H., 2017, *MNRAS*, 464, 1569
 Arnaboldi M., Neeser M. J., Parker L. C., Rosati P., Lombardi M., Dietrich J. P., Hummel W., 2007, *The Messenger*, 127, 28
 Baldry I. K. et al., 2010, *MNRAS*, 404, 86
 Baldry I. K. et al., 2018, *MNRAS*, 474, 3875
 Beaulieu J. P. et al., 2010, in Coudé du Foresto V., Gelino D. M., Ribas I., eds, ASP Conf. Ser. Vol. 430, Pathways Towards Habitable Planets. Astron. Soc. Pac., San Francisco, p. 266
 Bellstedt S. et al., 2020, preprint ([arXiv:2005.11917](https://arxiv.org/abs/2005.11917))
 Bertin E., 2010, SWarp: Resampling and Co-adding FITS Images Together, record 1010.068
 Bertin E., Arnouts S., 1996, *A&AS*, 117, 393

Bilicki M. et al., 2018, *A&A*, 616, A69
 Bremer M. N. et al., 2018, *MNRAS*, 476, 12
 Brown M. J. I. et al., 2014, *ApJS*, 212, 18
 Cardelli J. A., Clayton G. C., Mathis J. S., 1989, *ApJ*, 345, 245
 Davies L. J. M. et al., 2015, *MNRAS*, 452, 616
 Davies L. J. M. et al., 2017, *MNRAS*, 466, 2312
 Davies L. J. M. et al., 2018, *MNRAS*, 480, 768
 de Jong J. T. A. et al., 2013a, *The Messenger*, 154, 44
 de Jong J. T. A., Verdoes Kleijn G. A., Kuijken K. H., Valentijn E. A., 2013b, *Exp. Astron.*, 35, 25
 de Jong R. S. et al., 2019, *The Messenger*, 175, 3
 de Vaucouleurs G., de Vaucouleurs A., Corwin H. G., Jr, Buta R. J., Paturel G., Fouqué P., 1991, Third Reference Catalogue of Bright Galaxies. Volume I: Explanations and references. Volume II: Data for galaxies between 0^h and 12^h. Volume III: Data for galaxies between 12^h and 24^h. Springer, New York
 Deeley S. et al., 2017, *MNRAS*, 467, 3934
 Driver S. P. et al., 2011, *MNRAS*, 413, 971
 Driver S. P. et al., 2016a, *ApJ*, 827, 108
 Driver S. P., Davies L. J., Meyer M., Power C., Robotham A. S. G., Baldry I. K., Liske J., Norberg P., 2016b, *Astrophysics and Space Science Proceedings*, Vol. 42, *The Universe of Digital Sky Surveys*. Springer, p. 205
 Driver S. P. et al., 2016c, *MNRAS*, 455, 3911
 Driver S. P. et al., 2018, *MNRAS*, 475, 2891
 Driver S. P. et al., 2019, *The Messenger*, 175, 46
 Dunne L., Eales S., Ivison R., Morgan H., Edmunds M., 2003, *Nature*, 424, 285
 Eales S. et al., 2010, *PASP*, 122, 499
 Edge A., Sutherland W., Kuijken K., Driver S., McMahon R., Eales S., Emerson J. P., 2013, *The Messenger*, 154, 32
 Fitzpatrick E. L., 1999, *PASP*, 111, 63
 Gaia Collaboration, 2018, *A&A*, 616, A1
 Gehrels N., Spergel D., WFIRST SDT Project, 2015, *J. Phys. Conf. Ser.*, 610, 012007
 Girardi L. et al., 2012, *Astrophys. Space Sci. Proc.*, 26, 165
 González-Fernández C. et al., 2018, *MNRAS*, 474, 5459
 Hill R., Masui K. W., Scott D., 2018, *Appl. Spectrosc.*, 72, 663
 Hopkins A. M. et al., 2013, *MNRAS*, 430, 2047
 Hunter J. D., 2007, *Comput. Sci. Eng.*, 9, 90
 Ivezić Ž. et al., 2019, *ApJ*, 873, 111
 Jarrett T. H. et al., 2017, *ApJ*, 836, 182
 Keller S. C. et al., 2007, *PASA*, 24, 1
 Kelvin L. S. et al., 2012, *MNRAS*, 421, 1007
 Kelvin L. S. et al., 2014a, *MNRAS*, 439, 1245
 Kelvin L. S. et al., 2014b, *MNRAS*, 444, 1647
 Kuijken K. et al., 2019, *A&A*, 625, A2
 Lagos C. d. P. et al., 2019, *MNRAS*, 489, 4196
 Lange R. et al., 2016, *MNRAS*, 462, 1470
 Lara-López M. A. et al., 2013, *Astron. Nachr.*, 334, 466
 Lawrence A. et al., 2007, *MNRAS*, 379, 1599
 Leahy D. A. et al., 2019, *PASA*, 36, e024
 Lindegren L. et al., 2018, *A&A*, 616, A2
 Liske J. et al., 2015, *MNRAS*, 452, 2087
 Mahajan S. et al., 2018, *MNRAS*, 475, 788
 Martin D. C. et al., 2005, *ApJ*, 619, L1
 Milojević S., 2014, *Proc. Natl. Acad. Sci.*, 111, 3984
 Moffett A. J. et al., 2016a, *MNRAS*, 457, 1308

Moffett A. J. et al., 2016b, *MNRAS*, 462, 4336
 Neugebauer G. et al., 1984, *ApJ*, 278, L1
 Norris R. P. et al., 2011, *PASA*, 28, 215
 Pilbratt G. L. et al., 2010, *A&A*, 518, L1
 Planck Collaboration IX, 2013, *A&A*, 554, A139
 R Core Team, 2017, R: A Language and Environment for Statistical Computing, R Foundation for Statistical Computing, Vienna
 Robotham A. S. G. et al., 2011, *MNRAS*, 416, 2640
 Robotham A. S. G. et al., 2014, *MNRAS*, 444, 3986
 Robotham A. S. G., Taranu D. S., Tobar R., Moffett A., Driver S. P., 2017, *MNRAS*, 466, 1513
 Robotham A. S. G., Davies L. J. M., Driver S. P., Koushan S., Taranu D. S., Casura S., Liske J., 2018, *MNRAS*, 476, 3137
 Robotham A. S. G., Bellstedt S., Lagos C. d. P., Thorne J. E., Davies L. J., Driver S. P., Bravo M., 2020, *MNRAS*, 495, 905
 Schlafly E. F., Finkbeiner D. P., 2011, *ApJ*, 737, 103
 Skrutskie M. F. et al., 2006, *AJ*, 131, 1163
 Sutherland W. et al., 2015, *A&A*, 575, A25
 Vakili M. et al., 2019, *MNRAS*, 487, 3715
 Venemans B. P. et al., 2015, *MNRAS*, 453, 2259
 Voges W. et al., 1999, *A&A*, 349, 389
 Werner M. W. et al., 2004, *ApJS*, 154, 1
 Wright E. L. et al., 2010, *AJ*, 140, 1868
 Wright A. H. et al., 2016, *MNRAS*, 460, 765
 York D. G. et al., 2000, *AJ*, 120, 1579

APPENDIX A: PROFOUND COMMANDS

Here, we show the command used to run PROFOUND in the multiband mode for the detection phase: `profoundMultiBand` (

```
dir = input directory,
skycut = 2.0,
pixcut = 13,
ext = 1,
tolerance = 15,
reltol = -10,
cliptol = 100,
detectbands = c('r', 'z'),
multibands = c('r', 'z'),
keepsegims = TRUE,
magzero = c(0, 30),
dotot = FALSE,
docol = FALSE,
dogrp = FALSE,
verbose = TRUE,
boxiters = 4,
grid = c(50, 50),
roughpedestal = TRUE,
stats = FALSE,
groupstats = TRUE,
mask = 0,
app_diam = 1.4,
fluxtype = 'Jansky'
```

We also show the multiband call that was used to run the measurement phase after the regrouping of segments: `profoundMultiBand` (

```
segim = fixed_segim,28
dir = input directory,
iters_det = 6,
iters_tot = c(3, 3, 2, 2, 2, 2, 2, 2, 2, 2, 3, 3),
totappend = 't',
sizes_tot = c(15, 15, 5, 5, 5, 5, 5, 5, 5, 5, 5, 15, 15),
```

```
colappend = 'c',
detectbands = c('r', 'z'),
multibands = c('FUV', 'NUV', 'u', 'g', 'r', 'i', 'z', 'Y', 'J', 'H', 'K', 'W1', 'W2'),
keepsegims = TRUE,
magzero = c(18.82, 20.08, 0, 0, 0, 0, 30, 30, 30, 30, 30, 23.16, 22.82),
dotot = TRUE,
docol = TRUE,
dogrp = TRUE,
verbose = TRUE,
box = c(200, 200, 100, 100, 100, 100, 100, 100, 100, 100, 200, 200),
boxiters = 4,
boxadd = c(50, 50, 50, 50, 50, 50, 50, 50, 50, 50, 50, 50, 50),
grid = c(50, 50, 50, 50, 50, 50, 50, 50, 50, 50, 50, 50, 50),
roughpedestal = TRUE,
redosegim = FALSE,
deblend = FALSE,
groupstats = TRUE,
mask = 0,
SBdilate = 1.0,
SBN100 = 100,
app_diam = 1.4,
fluxtype = 'Jansky'
```

The following commands presents the manner in which we have run `profound` in the unresolved MIR–FIR regime, for each band separately: `profoundFitMagPSF` (

```
RAcen = RA coordinates,
Deccen = Dec coordinates,
image = sky-subtracted image,
header = image header,
psf = band PSF,
magzero = 23.24/19.6/8.9/8.9/11.68/11.67/11.62,28
magdiff = 5,
fit_iters = 5,
verbose = TRUE,
fluxtype = 'Jansky',
doProfound = TRUE,
findextra = TRUE,
itersub = TRUE,
```

²⁸Zero-points as stated in table 3 of Driver et al. (2016c).

```
pixcut = 3,  
skycut = 2,  
ext = 1,  
redosky = FALSE,  
iters = 4,  
tolerance = 0,  
sigma = 2/2/2/0/0/0,  
mask = 0,
```

```
psf.redosky = TRUE,  
boxiters = 2  
)
```

This paper has been typeset from a \LaTeX file prepared by the author.